

# An Ab Initio Multiple Cloning Method for Non-Adiabatic Excited-State Molecular Dynamics in NWChem

Huajing Song,\* Victor M. Freixas, Sebastian Fernandez-Alberti, Alexander J. White, Yu Zhang, Shaul Mukamel, Niranjana Govind,\* and Sergei Tretiak\*

Cite This: *J. Chem. Theory Comput.* 2021, 17, 3629–3643

Read Online

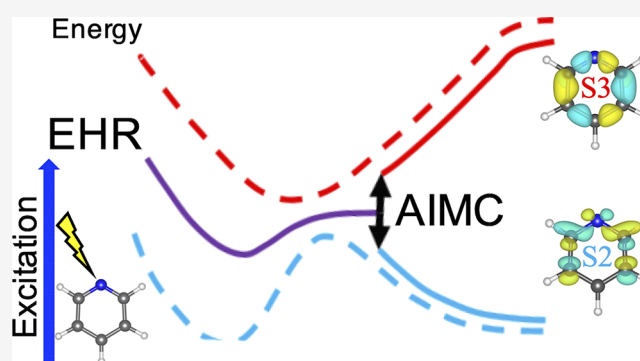
ACCESS |

Metrics & More

Article Recommendations

Supporting Information

**ABSTRACT:** The recently developed ab initio multiple cloning (AIMC) approach based on the multiconfigurational Ehrenfest (MCE) method provides a powerful and accurate way of describing the excited-state dynamics of molecular systems. The AIMC method is a controlled approximation to nonadiabatic dynamics with a particular strength in the proper description of decoherence effects because of the branching of vibrational wavepackets at a level crossing. Here, we report a new implementation of the AIMC algorithm in the open source NWChem computational chemistry program. The framework combines linear-response time-dependent density functional theory with Ehrenfest mean-field theory to determine the equations of motion for classical trajectories. The multidimensional wave function is decomposed into a superposition of Gaussian coherent states guided by Ehrenfest trajectories (i.e., MCE approach), which can clone with fully quantum mechanical amplitudes and phases. By using an efficient time-derivative based nonadiabatic coupling approach within the AIMC method, all observables are calculated on-the-fly in the nonadiabatic molecular dynamics process. As a representative example, we apply our implementation to study the ultrafast photoinduced electronic and vibrational energy transfer in a pyridine molecule. The effects of the cloning procedure on electronic and vibrational coherence, relaxation and unidirectional energy transfer are discussed. This new AIMC implementation provides a high-level nonadiabatic molecular dynamics framework for simulating photoexcited dynamics in complex molecular systems and experimentally relevant ultrafast spectroscopic probes, such as nonlinear coherent optical and X-ray signals.



## 1. INTRODUCTION

The electronic–vibrational dynamics involving nonadiabatic transitions<sup>1–3</sup> are fundamental to many photoinduced processes in chemistry and biochemistry, such as intraband relaxation,<sup>4,5</sup> energy transfer,<sup>6,7</sup> and light harvesting,<sup>8,9</sup> influenced by the spatial evolution of excitations, and transformation of photoexcitation energy into electrical energy via charge separation.<sup>10,11</sup> These processes commonly involve several coupled electronic excited states that introduce transient coherence effects, exciton self-trapping, differential intramolecular energy transfer pathways, and optically induced electronic density fluxes.<sup>12,13</sup> Trajectory-based mixed quantum-classical methods<sup>14,15</sup> are computationally efficient approaches for modeling nonadiabatic phenomena in the context of ab initio molecular dynamics. On the basis of the form of the adiabatic potential energy surface (PES) used to guide the trajectories, these quantum-classical methods are dominated by two distinct flavors,<sup>14,16,17</sup> the Ehrenfest mean-field (EHR)<sup>18</sup> and surface hopping (SH)<sup>19</sup> approaches.

In the SH approach, an ensemble of independent trajectories is propagated, where in each trajectory nuclei evolve along the

adiabatic/diabatic PES of the current electronic state. Nuclei are treated classically, while electrons are treated quantum mechanically, and transitions (hops) among coupled electronic states incorporate feedback between the electronic and nuclear subsystems. At the single trajectory level, detailed insights into mechanistic information can be gained, while observables such as excited-state lifetimes and energy or charge transfer rates are obtained from averages over many trajectories. The statistical ensemble of trajectories used in SH allows quantum yields<sup>20</sup> and branching ratios<sup>21</sup> to be determined quantitatively. Despite broad popularity in the community<sup>14,22–27</sup> and continuous improvements,<sup>28–31</sup> the SH methods essentially retain their ad hoc nature and description of many phenomena, such as coherences and some other quantum effects remain problem-

Received: February 4, 2021

Published: May 20, 2021



atic.<sup>19</sup> In our previous contribution, we have reported the ab initio SH implementation in NWChem.<sup>32</sup>

The EHR method, on the other hand, describes the evolution of trajectories in a mean-field sense, that is, governed by forces which are averaged over several PESs. The nonadiabatic molecular dynamics (NAMd) is then modeled by considering ensembles of uncoupled trajectories with different initial conditions. A more accurate approach is to solve the time-dependent Schrödinger equation using a set of trajectory-guided Gaussian basis functions (TBF), which optimize the number of necessary basis functions and cover the most important parts of the nuclear wave packet. Following this strategy, a multiconfigurational Ehrenfest (MCE)<sup>33</sup> dynamics approach, which is based on TBFs, following independent EHR trajectories, was introduced. While MCE employs Ehrenfest mean-field trajectories, the interaction between TBFs determines the evolution of their amplitudes, which is found by solving the time-dependent Schrödinger equation. The MCE approach provides a controlled approximation for NAMd converging to an exact solution in the limit of a complete TBF set. It has been successfully applied to simulate photoinduced processes in many molecular systems.<sup>34–36</sup>

Besides the MCE approach, there are other methods which use trajectory guided Gaussians for quantum dynamics such as the variational multiconfiguration Gaussian (vMCG) approach,<sup>37,38</sup> and the ab initio multiple spawning (AIMS) method.<sup>39,40</sup> The vMCG approach relies on coupled non-classical variational trajectories. Due to its computational cost and numerical instabilities, current vMCG implementations have only been tested for relatively small organic molecules. As an alternative, the AIMS method makes use of a much simpler choice for the evolution of the TBFs. The motion of the centers of Gaussians is determined classically on different electronic excited states. Throughout an AIMS simulation, the basis set is expanded (spawned) in an adaptive way according to transient couplings between states. AIMS has been shown to be accurate enough to reproduce spectroscopic measurements for a large variety of conjugated organic molecules.<sup>41,42</sup>

By balancing computational performance and accuracy, the MCE method is conceptually in between vMCG and AIMS. More importantly, the MCE approach retains an independent trajectory framework allowing for trivial parallelization, where interactions between the TBFs and subsequently the entire wave function for electronic and vibrational degrees of freedom are recovered through an inexpensive postprocessing. However, guiding the basis can become unphysical when two or more electronic states are significantly populated and the appropriate potential energy surfaces have significantly different gradients. In these situations, the average is no longer a faithful representation of the whole. The ab initio multiple cloning (AIMC)<sup>17,43,44</sup> algorithm was introduced to overcome this limitation. In the AIMC approach, the bifurcations of the wave function after leaving the nonadiabatic coupling region are taken into account through the cloning procedure: every time certain cloning conditions are fulfilled, the basis set is expanded by adding a new EHR guided TBF that have a non-zero Ehrenfest amplitude for only a single state, while the original TBF retains contributions of all other electronic states. Furthermore, as in SH methods, EHR approaches also lead to an incorrect treatment of decoherence phenomena.<sup>45,46</sup> The AIMC represents a natural extension to introduce decoherence in EHR simulations.

The original ab initio MCE and AIMC methods have been developed to be used in the adiabatic basis representation of electronic excited states.<sup>17,35</sup> Importantly, NAMd in large molecules can experience multiple trivial unavoids crossings between noninteracting states.<sup>47,48</sup> In such cases, the non-adiabatic couplings exhibit sharp peaks that are strongly localized at the exact crossing points and vanish elsewhere. Here, the wavepacket trajectory must follow the diabatic pathway of its parent wave function along the alternate adiabatic PES. Failure to follow the correct pathway can lead to unphysical sudden changes in the spatial localization of the current state.<sup>49</sup> In the MCE approach, the identity of adiabatic states during trivial unavoids crossings can change significantly within the Gaussian coherence state widths and the electronic overlaps must be properly taken into account. To deal with these situations, MCE in the time-dependent diabatic basis (MCE-TDDB)<sup>36</sup> was developed. In the MCE-TDDB approach, each Gaussian trajectory carries its own electronic basis, which is given by the adiabatic electronic states for the center of the Gaussian. As such, the overlaps between electronic states belonging to different trajectories are accounted for, and the amplitude swaps of electronic states at trivial unavoids crossings can be reproduced.<sup>33</sup>

Excited state NAMd of large systems frequently involves multiple energy relaxation pathways with wave function bifurcation,<sup>50</sup> where a combination of the MCE method with cloning algorithms (MCE-AIMC) becomes the method of choice. A series of previous works<sup>45,51</sup> report the implementation of the MCE-AIMC approach into the semiempirical<sup>52,53</sup> NEXMD program<sup>27</sup> and application to model dendritic molecules.<sup>54</sup> In this work, we present our implementation of the MCE-AIMC method in the NWChem computational chemistry package.<sup>55,56</sup> Building on our previously reported SH implementation in NWChem,<sup>32</sup> all excited state energies, gradients and nonadiabatic couplings are computed on-the-fly using linear-response time-dependent density functional theory (LR-TDDFT).<sup>57–63</sup> Numerical evaluation of the nonadiabatic coupling scalars<sup>30</sup> and an analytical method for calculating nonadiabatic coupling vectors<sup>29</sup> are an efficient combination for calculating the necessary ingredients for Ehrenfest approaches. Additionally, a state reassignment algorithm is implemented to handle trivial unavoids crossings.<sup>48</sup> We have used our NAMd implementation to study the ultrafast photoinduced unidirectional electronic and vibrational energy transfer in the pyridine molecule in the gas phase.

The rest of the paper is organized as follows. While the formalism has been presented in detail in previous works,<sup>17,35,45</sup> for completeness, we outline the theoretical methodology along with the working equations in section 2. Our new MCE-AIMC implementation is described in section 3. In section 4, we present and discuss the results of our simulations of photoexcited dynamics of pyridine, including a detailed analysis of the PES, evolution of the excited state populations, and vibrational coordinates coupled to the electronic energy transfer. Finally, we present our conclusions and outlook in section 5.

## 2. THEORETICAL METHODOLOGY

### 2.1. Ehrenfest Mean-Field Theory.

For Ehrenfest mean-field dynamics (EHR), the configuration  $n$  of a given molecular system is described by means of a wave function  $|\psi_n(t)\rangle$

$$|\psi_n(t)\rangle = |\chi_n(t)\rangle \sum_I a_I^{(n)}(t) |\phi_I^{(n)}\rangle \quad (1)$$

where  $|\chi_n(t)\rangle$  is the nuclear part given by a coherent state (CS)<sup>64</sup> moving along the classical mean-field, while the electronic part is spanned by the adiabatic basis  $|\phi_I^{(n)}\rangle$ .

In the coordinate representation, the CS is given by Gaussian functions centered on the Ehrenfest trajectories with coordinates  $\mathbf{R}_n$  and momenta  $\mathbf{P}_n$ :

$$|\chi_n(\mathbf{R}, t)\rangle = \left(\frac{2\alpha}{\pi}\right)^{N_{\text{dof}}/4} \times \exp(-\alpha(\mathbf{R} - \mathbf{R}_n)^2 + \frac{i}{\hbar} \mathbf{P}_n \cdot (\mathbf{R} - \mathbf{R}_n) + \frac{i}{\hbar} \gamma_n(t)) \quad (2)$$

where  $N_{\text{dof}}$  is the number of degrees of freedom of the system,  $\alpha$  is a width parameter, and  $\gamma_n$  is a phase. According to the tested parameters given by Thompson et al.,<sup>65</sup>  $\alpha = 4.7 \text{ Bohr}^{-2}$  for hydrogen atoms,  $\alpha = 22.7 \text{ Bohr}^{-2}$  for carbon atoms, and  $\alpha = 19.0 \text{ Bohr}^{-2}$  for nitrogen atoms, which will be used in the pyridine simulation (section 4). In the MD iteration, the phase  $\gamma_n$  is propagated semiclassically according to atomic velocity  $\dot{\mathbf{R}}_n$  and momenta  $\mathbf{P}_n$ . The kinetic part of the classical action,  $\dot{\gamma}_n$ , missing in eq 7 is written as

$$\dot{\gamma}_n = \frac{\mathbf{P}_n \cdot \dot{\mathbf{R}}_n}{2} \quad (3)$$

Since the kinetic part does not depend on the electronic degrees of freedom, it can be factorized out and inserted in eq 2. Finally, the motion of the centers of the Gaussians is given by the Hamilton equations:

$$\dot{\mathbf{R}}_n = M^{-1} \mathbf{P}_n \quad (4)$$

$$\dot{\mathbf{P}}_n = \mathbf{F}_n \quad (5)$$

and the active Ehrenfest force  $\mathbf{F}_n$  is calculated in a mean-field manner, with weighted contributions from all excited states and the coupling (NACR) between them (eq 42).

The time evolution of the Ehrenfest amplitudes,  $a_I^{(n)}$ , are dictated by the time-dependent Schrödinger equation:

$$\dot{a}_I^{(n)} = -\frac{i}{\hbar} V_I^{(n)} a_I^{(n)} - \sum_J \dot{\mathbf{R}}_n \cdot \mathbf{d}_{IJ} a_J^{(n)} \quad (6)$$

where  $\dot{\mathbf{R}}_n \cdot \mathbf{d}_{IJ}$  are the scalar nonadiabatic coupling terms (NACTs).<sup>32</sup> To avoid numerical inaccuracies associated with the fast phase oscillations of the complex  $a_I^{(n)}$  amplitudes in the first term of eq 6, we introduce a classical action,  $S_I^{(n)}$ , as

$$S_I^{(n)} = \int_0^t -V_I^{(n)} dt' \quad (7)$$

Here, we have deliberately omitted the kinetic part, which we already factorized out and inserted in eq 2,  $t'$  is the electronic time step between each atomic interval  $t \rightarrow t + \Delta t$ , with  $N_q = \Delta t/t'$  are the number of electronic steps per nuclear integration step. Then, the Ehrenfest amplitudes  $a_I^{(n)}$  are given as

$$a_I^{(n)} = \eta_I^{(n)} \exp\left(i \frac{S_I^{(n)}}{\hbar}\right) \quad (8)$$

Equations 7 and 8 are a change of variables introduced for numerical reasons. The phases of the electronic amplitudes  $a_I^{(n)}$  are calculated by the time-dependent Schrödinger equation (eq 6) have two contributions. The first one depends on the

excited state energies and the second one depends on the nonadiabatic couplings. The magnitudes of these two contributions are often very different. Equations 7 and 8 allow one to propagate these two contributions separately, avoiding numerical problems related to truncation errors when summing numbers of very different magnitude. Accordingly, eq 6 now can be solved by separating the time evolution of  $\eta_I^{(n)}$  into real  $\eta_{I,r}^{(n)}$  and imaginary  $\eta_{I,i}^{(n)}$  parts, which leads to the coupled equations:

$$\dot{\eta}_{I,r}^{(n)} = -\sum_J \dot{\mathbf{R}}_n \cdot \mathbf{d}_{IJ} \left[ \eta_{J,r}^{(n)} \cos\left(\frac{S_J - S_I}{\hbar}\right) - \eta_{J,i}^{(n)} \sin\left(\frac{S_J - S_I}{\hbar}\right) \right] \quad (9)$$

$$\dot{\eta}_{I,i}^{(n)} = -\sum_J \dot{\mathbf{R}}_n \cdot \mathbf{d}_{IJ} \left[ \eta_{J,i}^{(n)} \cos\left(\frac{S_J - S_I}{\hbar}\right) + \eta_{J,r}^{(n)} \sin\left(\frac{S_J - S_I}{\hbar}\right) \right] \quad (10)$$

with

$$\dot{S}_I^{(n)} = -V_I^{(n)} \quad (11)$$

## 2.2. Multiconfigurational Ehrenfest (MCE) Dynamics.

Multiconfigurational Ehrenfest (MCE) is a generalization of EHR where the wave function is written as a linear combination of Ehrenfest configurations, each of them moving along its own Ehrenfest (mean-field) trajectory.<sup>66</sup> In the MCE approach, the molecular wave function  $|\Psi(t)\rangle$  is expanded in a basis of TBFs  $|\psi_n(t)\rangle$  (eq 1) as

$$|\Psi(t)\rangle = \sum_n c_n(t) |\psi_n(t)\rangle \quad (12)$$

In the ab initio MCE approach,  $|\phi_I^{(n)}\rangle$  from the electronic part of eq 1 are adiabatic states,  $|\phi_I^{(n)}\rangle = |\phi_I(\mathbf{r}; \mathbf{R})\rangle$  that parametrically depend on the nuclear degrees of freedom and, thus, are the same for all TBFs. However, in extended poly atomic molecules,  $|\phi_I(\mathbf{r}; \mathbf{R})\rangle$  can change significantly with  $\mathbf{R}$  on the length scale of the nuclear Gaussian TBF widths, in particular, at trivial unavoided crossings.<sup>67,68</sup> An adiabatic representation becomes inappropriate in such situations. Instead, time-dependent diabatic electronic states are used that coincide with adiabatic states at the center of each Gaussian  $|\phi_I^{(n)}\rangle = |\phi_I(\mathbf{r}; \mathbf{R}_n(t))\rangle$ . The TDDB does not depend explicitly on  $\mathbf{R}$  and couplings between the states originate from their time-dependence through nuclei motion. The TDDB should not be confused with a diabatic basis, where different states are coupled through the off-diagonal matrix elements of the potential energy operator.

The equations of dynamics in the TDDB are similar to those in an adiabatic basis, except that the electronic states are now different for different TBFs, and the overlaps between them must be calculated and taken into account. When electronic states change smoothly, these overlaps are close to Kronecker's  $\delta_{IJ}$  for all pairs of TBFs with nonzero nuclear part overlap; in this case the TDDB approach is equivalent to an adiabatic approach. However, when adiabatic wave functions change sharply, for example, at trivial unavoided crossings, the overlap matrices will be significantly different, and the use of the TDDB ensures correct evolution of the whole wave function (eq 12) in the latter case.

The couplings between TBFs in the MCE approach are described by the time evolution of the amplitudes  $c_n$ , given by

eq 12. These amplitudes are calculated by substituting eq 12 into the time-dependent Schrödinger equation:

$$\sum_n \langle \psi_m | \dot{\psi}_n \rangle c_n = -\frac{i}{\hbar} \sum_n \left( H_{mn} - i\hbar \langle \psi_m | \frac{d\psi_n}{dt} \rangle \right) c_n \quad (13)$$

where

$$H_{mn} = \sum_{J,I} (a_J^{(m)})^* a_I^{(n)} \langle \chi_m \phi_J^{(m)} | (\hat{T} + \hat{V}) | \chi_n \phi_I^{(n)} \rangle \quad (14)$$

Similarly, overlaps in eq 13 include both nuclear part and electronic parts

$$\langle \psi_m(t) | \psi_n(t) \rangle = \langle \chi_m | \chi_n \rangle \sum_{I,J} (a_I^{(m)})^* a_J^{(n)} \langle \phi_I^{(m)} | \phi_J^{(n)} \rangle \quad (15)$$

nuclear kinetic energy matrix elements in eq 14 can be obtained analytically as

$$\langle \chi_m \phi_J^{(m)} | \hat{T} | \chi_n \phi_I^{(n)} \rangle = \langle \chi_m | -\frac{\hbar^2}{2} \nabla_{\mathbf{R}} M^{-1} \nabla_{\mathbf{R}} | \chi_n \rangle \langle \phi_I^{(m)} | \phi_J^{(n)} \rangle \quad (16)$$

while the potential energy matrix elements are approximated using the generalized first-order bra-ket averaged Taylor equation.<sup>17,36</sup> For implementation, the expression is rewritten as,<sup>45</sup>

$$\begin{aligned} \langle \chi_m \phi_J^{(m)} | \hat{V} | \chi_n \phi_I^{(n)} \rangle &= \frac{1}{2} \langle \phi_I^{(m)} | \phi_J^{(n)} \rangle \langle \chi_m | \chi_n \rangle \\ &\left\{ (V_I^{(m)} + V_J^{(n)}) + \frac{i}{4\alpha\hbar} (\mathbf{P}_n - \mathbf{P}_m) \cdot (\nabla_{\mathbf{R}} V_I^{(m)} + \nabla_{\mathbf{R}} V_J^{(n)}) \right. \\ &\left. - \frac{1}{2} (\mathbf{R}_m - \mathbf{R}_n) \cdot (\nabla_{\mathbf{R}} V_I^{(m)} - \nabla_{\mathbf{R}} V_J^{(n)}) \right\} \quad (17) \end{aligned}$$

Finally, eq 13 reflecting the time-dependence of TBFs is evaluated as

$$\begin{aligned} \left\langle \psi_m \left| \frac{d\psi_n}{dt} \right. \right\rangle &= \left\langle \chi_m \left| \frac{d\chi_n}{dt} \right. \right\rangle \sum_{I,J} \langle \phi_I^{(m)} | \phi_J^{(n)} \rangle (a_I^{(m)})^* a_J^{(n)} \\ &- \frac{i}{\hbar} \langle \chi_m | \chi_n \rangle \sum_{I,J} \langle \phi_I^{(m)} | \phi_J^{(n)} \rangle (a_I^{(m)})^* a_J^{(n)} V_J^{(n)} \quad (18) \end{aligned}$$

where

$$\begin{aligned} \left\langle \chi_m \left| \frac{d\chi_n}{dt} \right. \right\rangle &= \dot{\mathbf{R}}_n \langle \chi_m | \frac{d}{d\mathbf{R}_n} | \chi_n \rangle + \dot{\mathbf{P}}_n \langle \chi_m | \frac{d}{d\mathbf{P}_n} | \chi_n \rangle \\ &+ \frac{i}{\hbar} \dot{\gamma}_n \langle \chi_m | \chi_n \rangle \quad (19) \end{aligned}$$

In the adiabatic formulation, the kinetic energy operators yield nonadiabatic coupling terms that include both first and second-order derivatives with respect to the nuclear coordinates. Neglecting the second-order derivative is an approximation that is often questioned. However, this is not the case for the TDDb, where the nonadiabatic coupling arises from the time dependence of the electronic basis function, so the second derivative term with respect to the nuclear coordinates does not appear and no additional approximation is needed.<sup>69</sup>

The overlaps  $\langle \phi_I^{(m)} | \phi_J^{(n)} \rangle$  between the electronic parts of different TBFs can be calculated directly. We have found that propagating the electronic overlaps together with the basis can

significantly improve the simulation efficiency and reduce the numerical error, especially in the large molecular systems.

$$\begin{aligned} \frac{d}{dt} \langle \phi_I^{(m)} | \phi_J^{(n)} \rangle &= \dot{\mathbf{R}}_m \cdot \sum_K \langle \phi_K^{(m)} | \phi_J^{(n)} \rangle \mathbf{d}_{KI}^{(m)} \\ &+ \dot{\mathbf{R}}_n \cdot \sum_K \langle \phi_I^{(m)} | \phi_K^{(n)} \rangle \mathbf{d}_{KJ}^{(n)} \quad (20) \end{aligned}$$

We note that such an approach may slightly overestimate the electronic overlaps,<sup>45</sup> but the accuracy is compatible with other approximations used in the TDDFT framework. However, the propagation of overlaps, as well as the propagation of Ehrenfest amplitudes  $a_j$ , still cannot reproduce instant swaps of electronic states at trivial unavoided crossings.<sup>36</sup> To take these swaps into account, we track the identity of the adiabatic states by analyzing the overlaps  $\langle \phi_I(t) | \phi_J(t + \Delta t) \rangle$  between consecutive adiabatic states at  $t$  and  $t + \Delta t$  using the Min Cost algorithm<sup>47</sup> and swap the states when necessary.<sup>48</sup> This includes both the swap of Ehrenfest amplitudes and the appropriate change of overlaps with their phase (+, -) in eq 20, so that the total wave function remains conserved.

**2.3. AIMC Algorithm.** The Ehrenfest basis set is guided by an average potential, accurate for dynamical processes, where the coupling between states persists in time between nearly parallel PES, but it can be unphysical when the PES of two or more populated electronic states become different in shape, which leads to wave packet branching after leaving the nonadiabatic coupling region. To deal with these cases, the AIMC algorithm<sup>17,45</sup> is applied as follows: the original basis set of TBFs is expanded by "cloning" one TBF into two copies in a way that does not alter the original wave function. This is done by creating one of the clones  $|\psi_{n_1}\rangle$  in a pure state and the other clone  $|\psi_{n_2}\rangle$ , which includes contributions from all other electronic states

$$|\psi_{n_1}\rangle = |\chi_n\rangle \left( \frac{a_I^{(n)}}{|a_I^{(n)}|} \times |\phi_I^{(n)}\rangle + \sum_{J \neq I} 0 \times |\phi_J^{(n)}\rangle \right) \quad (21)$$

$$|\psi_{n_2}\rangle = |\chi_n\rangle \left( 0 \times |\phi_I^{(n)}\rangle + \frac{1}{\sqrt{1 - |a_I^{(n)}|^2}} \sum_{J \neq I} a_J^{(n)} |\phi_J^{(n)}\rangle \right) \quad (22)$$

Then, the corresponding MCE amplitudes for these two new TBFs are set to

$$c_{n_1} = c_n |a_I^{(n)}| \quad (23)$$

$$c_{n_2} = c_n \sqrt{1 - |a_I^{(n)}|^2} \quad (24)$$

such that the contribution of the two clones  $|\psi_{n_1}\rangle$  and  $|\psi_{n_2}\rangle$  to the original wave function eq 12 remains conserved.

$$c_n |\psi_n\rangle = c_{n_1} |\psi_{n_1}\rangle + c_{n_2} |\psi_{n_2}\rangle \quad (25)$$

During the dynamics, each TBF can clone several times to enlarge the basis set sampling by branching a trajectory into two, which will also double the computational cost. Meanwhile, the contribution of each new clone to the whole wave function decreases with the cloning times because of the rescaling of the amplitudes (see eq 24). Despite the integral contribution of these low-amplitude trajectories being significant, further cloning would be inefficient, as far as an

effect per cloning event is concerned. Thus, defining proper criteria to restrict cloning events is critical to balance computational efficiency and the final accuracy of the results. These criteria should allow for cloning throughout the simulation whenever the Ehrenfest approximation fails to lead to the correct outcome of the process. Besides, they should also be general enough so that they are defined according to the relative magnitudes and directions of the different components of the Ehrenfest force. Consequently, the thresholds for such criteria do not need to be reoptimized every time, as they are weakly sensitive to the molecular system or the number of excited states involved in the process under study. Based on previous experience<sup>17,45</sup> and continuous improvement over case studies, we have defined three general cloning criteria:

**Criterion 1.** Cloning events should take place only when at least two adiabatic electronic states are sufficiently populated. The number of populated electronic excited states can be monitored by the distribution width  $W^{(n)}$  for the amplitudes of electronic wave function  $|\phi_I^{(n)}\rangle$  in eq 1 as

$$W^{(n)} = \frac{1}{\sum_I |a_I^{(n)}|^4} \quad (26)$$

When  $W^{(n)} \approx 1$ , electrons are concentrated on a single electronic excited state. Values of  $W^{(n)} \approx N$  indicate a uniform distribution of electrons among all  $N$  states. Therefore, by restricting cloning events to situations, in which  $W^{(n)} > 2$  will guarantee that at least two electronic excited states are significantly populated.

**Criterion 2.** Cloning events should prevent situations in which the nuclear motion is guided by the unphysical average Ehrenfest force. In such cases, the Ehrenfest TBF could fail to explore dynamically important regions of the configurational space. Following the original idea of the breaking force introduced by Makhov et al.,<sup>17</sup> the mismatch between the Ehrenfest weighted average force  $\mathbf{F}_M^{(n)} = -\sum_I |a_I^{(n)}|^2 \nabla_{\mathbf{R}_n} V_I^{(n)}$  (first term in eq 42) and the force  $\mathbf{F}_{max}^{(n)}$  evaluated on the most populated state is defined by a pseudoangle  $\theta^{(n)}$  as

$$\theta^{(n)} = \arccos\left(\frac{2\mathbf{F}_M^{(n)} \cdot \mathbf{F}_{max}^{(n)}}{|\mathbf{F}_M^{(n)}|^2 + |\mathbf{F}_{max}^{(n)}|^2}\right) \quad (27)$$

This definition of  $\theta^{(n)}$  takes into account the difference in both directions and magnitudes between  $\mathbf{F}_M^{(n)}$  and  $\mathbf{F}_{max}^{(n)}$ . In the case when both magnitudes are equivalent,  $\theta^{(n)}$  is reduced to a standard definition of the angle between two vectors. Note that, this criterion only accounts for the contributions of the gradients of each adiabatic state to the Ehrenfest force (first term in eq 42) but does not consider the nonadiabatic contributions. Thus, it is suitable to identify situations, in which the average Ehrenfest force lacks physical meaning, as the different adiabatic forces move nuclei in a bifurcated way. By defining a criterion 2 threshold,  $\theta^{(n)} > \pi/12$ , the activated cloning event will amend the unphysical nuclear motion driven by different adiabatic forces toward a bifurcation.

**Criterion 3.** The cloned phase space should be restricted within regions, where the electronic states are not strongly coupled to limit the rate of basis set growth. Otherwise, a TBF would clone multiple times while passing through a conical intersection. These regions are evaluated by weighting the scalar nonadiabatic coupling (NACTs) with the real part of

electronic amplitude ratio between each excited state and the most populated state

$$\delta^{(n)} = \sum_I \left| \operatorname{Re}\left(\frac{2a_I^{(n)}}{a_{max}^{(n)}}\right) \times \mathbf{R} \cdot \mathbf{d}_{(I,max)} \right| \quad (28)$$

The three cloning criteria have been chosen to be mostly independent of the molecular system under study but may need to be adjusted as needed. Outside certain limits, inadequate values of these criteria can lead either to computationally intractable growth in the number of TBFs or to avoiding cloning events altogether.

**2.4. Observables.** On the basis of the MCE,<sup>36,45</sup> the expectation value of any operator acting on the electronic subspace can be calculated in the following form,

$$\langle \hat{N} \rangle = \operatorname{Re}\left\{ \sum_{m,n} c_m^* c_n \langle \chi_n | \chi_m \rangle \times \sum_{I,J,K} (a_I^{(m)})^* a_J^{(n)} \langle \phi_K^{(m)} | \phi_J^{(n)} \rangle N_{IK}^{(m)} \right\} \quad (29)$$

in which

$$N_{IK}^{(m)} = \langle \phi_I^{(m)} | \hat{N} | \phi_K^{(n)} \rangle \quad (30)$$

Accordingly, electronic state populations can be calculated by substituting the adiabatic population operator  $\hat{P}_K = |\phi_K^{(n)}\rangle \langle \phi_K^{(n)}|$  to  $\hat{N}$  in eqs 29 and 30 to obtain

$$\langle \hat{P}_K \rangle = \operatorname{Re}\left\{ \sum_{m,n} c_m^* c_n \langle \chi_n | \chi_m \rangle (a_K^{(m)})^* \sum_I a_I^{(n)} \langle \phi_K^{(m)} | \phi_I^{(n)} \rangle \right\} \quad (31)$$

The multiconfigurational molecular wave function is expanded as

$$|\Psi\rangle = \sum_n c_n |\chi_n\rangle \sum_I a_I^{(n)} |\phi_I^{(n)}\rangle \quad (32)$$

which is a combination of the EHR (eq 1) and the MCE (eq 12) equations, respectively. Meanwhile, the effective Hamiltonian matrix eq 14 is constructed using the kinetic energy, eq 16, and potential energy, eq 17, matrix elements acting on the electronic subspace. Then, the expected MCE kinetic energy is obtained as

$$\langle \Psi | \hat{T} | \Psi \rangle = \left\{ \sum_{m,n} c_m^* c_n \langle \chi_m | \hat{T} | \chi_n \rangle \sum_{I,J} (a_I^{(m)})^* a_J^{(n)} \langle \phi_I^{(m)} | \phi_J^{(n)} \rangle \right\} \quad (33)$$

here only the adiabatic approximation ( $\hat{T}|\phi_I^{(n)}\rangle \approx 0$ ) is taken into account and the matrix element  $\langle \chi_m | \hat{T} | \chi_n \rangle$  is obtained analytically by eq 16 with

$$\begin{aligned} \langle \chi_m | \nabla_{\mathbf{R}}^2 | \chi_n \rangle = & \left( -\alpha + \alpha^2 (\mathbf{R}_n - \mathbf{R}_m)^2 - \frac{1}{4\hbar^2} (\mathbf{P}_n + \mathbf{P}_m)^2 \right. \\ & \left. + \frac{i}{\hbar} \alpha (\mathbf{P}_n + \mathbf{P}_m) \cdot (\mathbf{R}_n - \mathbf{R}_m) \right) \times \langle \chi_m | \chi_n \rangle \end{aligned} \quad (34)$$

Similarly, the expected MCE potential energy is written as

$$\langle \Psi | \hat{V} | \Psi \rangle = \operatorname{Re}\left\{ \sum_{n,m} c_n c_m^* \sum_{I,J} (a_I^{(m)})^* a_J^{(n)} \langle \chi_m | \phi_I^{(m)} | \hat{V} | \phi_J^{(n)} | \chi_n \rangle \right\} \quad (35)$$

where the matrix element  $\langle \chi_m \phi_I^m | \hat{V} | \phi_I^n \chi_n \rangle$  is calculated as eq 17.

Our current implementation of the MCE approach utilizes DFT and LR-TDDFT to evaluate the electronic energies and nonadiabatic couplings. Both RPA<sup>58,62</sup> and the Tamm–Dancoff approximation (TDA, also known as CIS)<sup>70</sup> are available to the LR-TDDFT calculation. Within the TDA approximation, the CIS eigenstates, written in the atomic orbital (AO) basis, are frequently denoted as transition density matrices (or electronic normal modes) and can be formally written as<sup>27,31</sup>

$$(\rho_I^{(n)})_{i,j} = \langle \phi_I^{(n)} | \hat{c}_i^\dagger \hat{c}_j | \phi_g^{(n)} \rangle \quad (36)$$

where  $|\phi_g^{(n)}\rangle$  is the ground state wave function, and  $\hat{c}_i^\dagger$  and  $\hat{c}_j$  are the electron creation and annihilation operators, respectively, with subscripts  $i$  and  $j$  referring to the AO basis functions. Diagonal elements  $(\rho_I^{(n)})_{i,i}$  are relevant to the changes in the distribution of electronic density on the  $i$ th orbital in the case of bound excitonic states caused by excitation.<sup>71</sup>

During the dynamics, the intramolecular electronic energy redistribution can be followed by the time-dependent spatial localization of  $\rho_I^{(n)}$ . Generally, to describe cases of tightly bound Frenkel and charge-transfer delocalized Wannier excitons, the entire transition density matrix needs to be analyzed.<sup>71,72</sup> However, in cases of localized Frenkel-type excitons with relatively weak charge transfer character, an analysis of the diagonal part suffices. In such cases, the fraction of  $\rho_I^{(n)}$  localized on a specific segment or chromophore unit  $X$  can be defined as

$$\rho_{I,X}^{(n)} = \frac{\sum_{i \in X} (\rho_I^{(n)})_{i,i}^2}{\sum_i (\rho_I^{(n)})_{i,i}^2} \quad (37)$$

with the operator  $\hat{\rho}_X$  such that

$$\hat{\rho}_X |\phi_I^{(n)}\rangle = \rho_{I,X}^{(n)} |\phi_I^{(n)}\rangle \quad (38)$$

and substituting it into eq 29 to obtain

$$\langle \hat{\rho}_X \rangle = \text{Re} \left\{ \sum_{m,n} c_m^* c_n \langle \chi_m | \chi_n \rangle \sum_{I,J} (a_I^{(m)})^* a_J^{(n)} \langle \phi_I^{(m)} | \phi_J^{(n)} \rangle \rho_{I,X}^{(m)} \right\} \quad (39)$$

In a similar way, the expectation value of the atomic distances between  $i$  and  $j$  of the molecule  $R_{ij} = |\mathbf{R}^{(i)} - \mathbf{R}^{(j)}|$  can be approximated as

$$\langle R_{ij} \rangle \approx \left| \sum_{m,n} c_m^* c_n (\langle \chi_n | \mathbf{R}^{(i)} | \chi_m \rangle - \langle \chi_n | \mathbf{R}^{(j)} | \chi_m \rangle) \times \sum_{I,J} (a_I^{(n)})^* a_J^{(m)} \langle \phi_I^{(m)} | \phi_J^{(n)} \rangle \right| \quad (40)$$

by assuming that the oscillations of the distance between atoms are usually much smaller than the distance itself. Using the expression for matrix elements  $\langle \chi_n | \mathbf{R}^{(i)} | \chi_m \rangle$ <sup>17</sup> and taking into account the imaginary part of all matrix elements, it vanishes with the double sum running over scripts  $m$  and  $n$ ; eq 40 takes the form

$$\langle R_{ij} \rangle \approx \text{Re} \left\{ \sum_{m,n} c_m^* c_n \langle \chi_m | \chi_n \rangle \left[ \left( \frac{\mathbf{R}_n^{(i)} + \mathbf{R}_m^{(i)}}{2} \right) - \left( \frac{\mathbf{R}_n^{(j)} + \mathbf{R}_m^{(j)}}{2} \right) \right] \times \sum_{I,J} (a_I^{(n)})^* a_J^{(m)} \langle \phi_I^{(m)} | \phi_J^{(n)} \rangle \right\} \quad (41)$$

with  $\mathbf{R}_n^{(i)}$  is the coordinate vector for the center of the  $n$ th Gaussian TBF on the  $i$ th atom.

### 3. MCE-AIMC IMPLEMENTATION

In this section, we detail our implementation of the MCE-TDDB method<sup>36</sup> and the AIMC algorithm build up on the TDDFT level in NWChem.<sup>55,56</sup> Following our SH<sup>32</sup> implementation in NWChem, the new LR-TDDFT based MCE-AIMC method also includes advanced features developed for the AIMC algorithm<sup>45</sup> in the semiempirical NEXMD program.<sup>27</sup> Both AIMC and MCE capabilities functions have been implemented within the same NAMM framework in NWChem for on-the-fly quantum molecular dynamics simulations. In the MCE-AIMC framework, the adiabatic energies of electronic states ( $V$ ), nuclear forces ( $\mathbf{F}$ ), and nonadiabatic couplings vectors ( $\mathbf{d}$ ) are a required input, which is computed using (TD)DFT. Ground state properties are determined from ground state DFT. Excitation energies are determined from linear response, excited-state forces are calculated based on quadratic response function, and derivative nonadiabatic couplings between two excited electronic states are determined from the pseudowave function. Both full linear response TDDFT based on the random phase approximation (RPA) and the Tamm–Dancoff approximation (TDA) can be used to evaluate gradients and couplings for restricted singlet or triplet, and unrestricted calculations. Available (TD)DFT functionals and accuracy analysis can be found in a series of our previous publications.<sup>63,70,73</sup>

The MCE-AIMC NAMM has been implemented as an extension to the quantum molecular dynamics (QMD) module<sup>74</sup> in NWChem. The workflow is as follows: For each time step, a ground state DFT calculation is first performed. This is followed by a LR-TDDFT calculation (either RPA or TDA) of the adiabatic excited states, excitation energies, gradients and transition density matrices. Derivative nonadiabatic coupling scalars NACT (formally defined as  $\hat{\mathbf{R}}_i \cdot \mathbf{d}_{IJ}$ ) are determined directly using the pseudowave function approach.<sup>75</sup> Here,  $\hat{\mathbf{R}}_i$  is a nuclear velocity and the nonadiabatic coupling vector (NACR)<sup>32</sup> between the  $I$ th and  $J$ th adiabatic states with wave functions  $\phi_I(\mathbf{R})$  and  $\phi_J(\mathbf{R})$ , respectively, is given by  $\mathbf{d}_{IJ} = \langle \phi_I(\mathbf{R}) | \nabla_{\mathbf{R}} \phi_J(\mathbf{R}_n) \rangle$ . Notably,  $\mathbf{d}_{IJ}$  is required for EHR in each nuclear time step, which is calculated analytically.<sup>29</sup> Details of the implementation for computing NACT and NACR are given in ref 32. The time-dependent Schrödinger equation is propagated by the fourth-order Runge–Kutta<sup>76</sup> algorithm, and the nuclei are propagated forward using the velocity Verlet method.<sup>77</sup>

The NACT scalars and Ehrenfest amplitudes  $a_I(t)$  in eq 6 are highly oscillating quantities that require re-evaluation at smaller electronic time steps,  $\delta t$ , compared with standard nuclear time steps,  $\Delta t$  (i.e.,  $\delta t < \Delta t$ ). The chosen value of  $\delta t$  must be small enough to capture the rapidly changing  $a_I(t)$ , for example, near conical intersections, to avoid numerical errors between cloned configurations.<sup>69</sup> A detailed analysis of deviation in the sum of populations across all MCE states

related to the electronic time steps can be found in SI. Therefore, the nuclear time step interval is split up into  $N_q$  time steps with  $\delta t = \Delta t/N_q$  ( $N_q = 10-100$ ). Then, eqs 7–11 are propagated with smaller electronic time steps  $t + k\delta t$  ( $k = 0, \dots, N_q - 1$ ), using a simple linear interpolation and extrapolation scheme to obtain the electronic energies  $V_I$  and NACT couplings  $\mathbf{R}_n \cdot \mathbf{d}_{IJ}$ .

The interaction between the nuclear and electronic parts in EHR (eq 1) is given by a mean-field with a weighted contribution from all excited states and the couplings between them. The EHR force  $\mathbf{F}_n$  driving the configuration  $n$  with  $\mathbf{R}_n$  is given by

$$\mathbf{F}_n = - \sum_I |a_I^{(n)}|^2 \nabla_{\mathbf{R}_n} V_I^{(n)} + \sum_{IJ} (a_I^{(n)})^* a_J^{(n)} \mathbf{d}_{IJ}^{(n)} (V_I^{(n)} - V_J^{(n)}) \quad (42)$$

where  $V_I^{(n)} = V_I(\mathbf{R}_n)$  is the  $I$ th adiabatic PES. The first term in right side of eq 42 is a sum of gradients for all electronic states weighted according to their Ehrenfest populations  $|a_I^{(n)}|^2$ . In practice, the weight  $|a_I^{(n)}|^2$  of certain PES can be very small at some moments, the contribution of such PES to the mean-field forces is negligible. Accordingly, in the pure EHR method (without the cloning algorithm) the gradient calculation on the adiabatic states with populations  $|a_I^{(n)}|^2 < 10^{-3}$  are skipped to save computational time. Usually, this strategy leads to errors less than 0.1% by assuming the gradients of each PES are of the same order of magnitude. However, in the MCE-AIMC method, the calculation of the potential energy matrix elements in eq 17 requires the gradients from all adiabatic states, a step that cannot be simplified. The last term in eq 42 represents the nonadiabatic contribution to the force and is consistent with the time evolution of the Ehrenfest amplitudes  $a_I^{(n)}$  from the time-dependent Schrödinger equation eq 6.

The key quantities in the present approach is a set of single-electron density matrices, eq 36, and  $\rho_{00}$  is defined as the ground-state density matrix. The eigenfunction of the tetradic Liouville operator  $L$  ( $L\xi_I = \Omega_I \xi_I$ )<sup>71,78</sup> in LR-TDDFT approach corresponds to the transition density matrix  $\xi_I \equiv \rho_I$  for the ground to excited state transition  $|0\rangle \rightarrow |I\rangle$ . The respective eigenvalue  $\Omega_I$  is the respective electronic transition energy such that the excited state energy of state  $I$  is given by the ground state SCF energy plus the transition energy as  $V_I = V_0 + \Omega_I$ . Importantly, the transition density matrices  $\xi_I$ , as eigenvectors, may change (albeit rarely) their sign between two trajectory points (i.e.,  $\xi_I(t) \sim -\xi_I(t + \Delta t)$ ) yielding inconsistent NACR and NACTs values.<sup>27</sup> However, the QMD propagation in NWChem tracks the relative phase of the transition density matrices at each time step. Since  $\xi_I(t)$  and  $\xi_I(t + \Delta t)$  are eigenvectors of  $L$ , they obey the normalization condition  $\langle \xi_I | \xi_I \rangle = \delta_{II}$ , where  $\delta_{II}$  is the Kronecker delta. Therefore, if  $\langle \xi_I(t) | \xi_I(t + \Delta t) \rangle < 0$ , then the sign of  $\xi_I(t + \Delta t)$  is changed to preserve consistency at the next time-step.

To start the MCE-AIMC NAMD simulation, trajectories are typically initiated by equilibrating the system in ground-state ab initio molecular dynamics. The initial sampling of the conformational space should be adequate to represent the equilibrated ensemble of molecules at the given thermodynamic conditions, which may be achieved using different thermostat models. In the current study, the stochastic velocity rescaling thermostat<sup>79</sup> is applied to achieve the canonical ensemble for the initial ground-state sampling. The subsequent MCE-AIMC NAMD simulations can be run either at constant energy or constant temperature. We found that the velocity

rescaling thermostat introduces numerical errors between cloned trajectories (see SI section 1), thus, the microcanonical (NVE) ensemble is used in the MCE-AIMC NAMD stage.

After assigning the initial conditions (i.e., taking snapshots of nuclear coordinates/velocities from the ground state dynamics and promoting each configuration to a specific excited state), the MCE-AIMC NAMD algorithm in NWChem propagates an ensemble of trajectories in parallel. In particular, it calculates each trajectory as follows:

1. For an initial time step, nuclei are propagated with the gradient along the initial adiabatic electronic state  $I$ th.
2. At the new position, the adiabatic gradients  $-\nabla_{\mathbf{R}_n} V_I^{(n)}(\mathbf{R})$ , state energies  $V_I = V_0 + \Omega_I$ , and the transition density matrices  $\xi_I$  for all excited-states  $I$  included in simulations are evaluated for the time step  $t + \delta t$ .
3. Phases of the transition density matrices are tracked and appearance of the trivial unavoided crossings is checked with the Min-Cost algorithm. NACRs ( $\mathbf{d}_{IJ}$ ) and NACTs ( $\mathbf{R} \cdot \mathbf{d}_{IJ}$ ) between all pairs of excited-states are computed as well. If a trivial crossing  $I/J$  is detected, the states are reassigned by interchanging their Ehrenfest amplitudes  $a_I^{(n)}/a_J^{(n)}$  and the electronic overlaps  $\langle \phi_I^m | \phi_J^{(n)} \rangle$  in eq 20, and the couplings are set to zero ( $\mathbf{d}_{IJ} = 0$ ) for states involved in the trivial crossing.
4. The coefficients  $a_I^{(n)}$  (eqs(7)-(11)) and the overlaps  $\langle \phi_I^m | \phi_J^{(n)} \rangle$  (eq 20) are propagated at the  $N_q$  electronic time step intervals  $[t + k\delta t, t + (i + 1)\delta t]$  ( $k = 0, \dots, N_q - 1$ ). Within the intermediate times ( $\delta t$ ), both of the energies and NACTs are propagated with a linear assumption and the coefficients  $a_I^{(n)}$  are calculated by a linear interpolated fourth-order Runge–Kutta propagator. Then, the active Ehrenfest force  $\mathbf{F}_n$  in nuclear time steps ( $\Delta t$ ) is calculated by eq 42.
5. The cloning criteria 1–3 (eqs 26–28) are then evaluated. If cloning conditions are fulfilled, the basis set is expanded by adding a new TBF that has nonzero Ehrenfest amplitude for only a single state, while the original TBF retains contributions of all other electronic states (eqs 21 and 22). At the cloning moment, both trajectories contain the same coordinates, velocities, and gradients.
6. If the system contains more than one configuration (i.e., cloned trajectories), steps 2–5 will be repeated for all configurations within the same time step.
7. The MCE process is performed to propagate the MCE amplitudes  $c_n$  and calculate all the observables.
8. The nuclei are propagated according to the Ehrenfest force  $\mathbf{F}_n$  by the velocity Verlet algorithm. The relevant data are stored and the code returns to step 2 for the next time step.

#### 4. EXCITED-STATE RELAXATION OF PYRIDINE

The photoinduced dynamics of pyridine in the gas phase is simulated to validate and demonstrate our implementation of the MCE-AIMC method. Four sets of calculations with different exchange-correlation (XC) functionals and basis sets (PBE0<sup>80</sup>/STO-3G,<sup>81</sup> PBE0/Def2-SVP,<sup>82</sup> B3LYP<sup>83</sup>/STO-3G, and B3LYP/Def2-SVP) were performed to evaluate the behavior of AIMC with different exchange-correlation functionals and basis set combinations. The minimal STO-3G basis sets is included as a test case with respect to the more accurate

Def2-SVP basis providing a useful comparison for the NAMD results.

Natural transition orbitals (NTOs) and band gaps are analyzed based on the ground-state optimized structures using different XC functionals and basis sets, respectively. Table 1

**Table 1. Comparison of the Vertical Excitation Energies (in eV) for the First Three Singlet Excited States of Pyridine**

method	$S_1$	$S_2$	$S_3$
PBE0/STO-3g	5.25	5.60	6.46
PBE0/Def2-SVP	4.89	5.10	5.78
B3LYP/STO-3g	5.09	5.36	6.22
B3LYP/Def2-SVP	4.80	4.98	5.66
CASSCF <sup>88</sup>	5.04	5.26	5.96
CASPT2 <sup>89</sup>	4.89	5.00	5.25
exp. spectrum <sup>89</sup>	4.90	5.13	5.52

compares the vertical excitation energies calculated by different methods using LR-TDDFT/Tamm–Dancoff approximation (TDA).<sup>70</sup> As expected, a smaller basis results in blue-shifted energies compared with the extended basis. Since both hybrid functionals have similar fractions of Hartree–Fock exchange (20% in B3LYP and 25% in PBE0), the computed results are similar. Based on a series of NAMD studies,<sup>28,84,85</sup> the excited state PESs from hybrid TDDFT are considerably more accurate than those from nonhybrid TDDFT. In a recent (TD)DFT study,<sup>86</sup> the mean unsigned errors for valence excitations in small organic molecules were 0.22 eV by PBE0 and 0.20 eV by B3LYP. Our results based on the Def2-SVP (0.1 eV by PBE0 and 0.13 eV by B3LYP) show reasonable accuracy in excitation energies calculation. More importantly, the energy gaps between excited states need to be calculated very accurately, which is critical for the relaxation rates during the excited states dynamics.<sup>87</sup> Overall, all computed results agree reasonably well with excitation energies measured experimentally. In practice, one should carefully consider the electronic structure methodology based on the specific molecular system in practice.

Figure 1 shows the characteristic NTOs for the first three singlet excited-states of pyridine evaluated at the ground-state optimal geometry computed with PBE0/Def2-SVP method. Combining with the oscillator strength analysis, the lowest-lying excited state ( $S_1$ ) is an optically allowed (bright)  $n - \pi^*$  transition dominated by a single electron–hole NTO transition (99%). The second excited-state ( $S_2$ ), on the other hand, is an optically forbidden (dark)  $n - \pi^*$  transition. Finally, the third excited-state ( $S_3$ ) is optically allowed  $\pi - \pi^*$  excitation dominated by 2 NTOs transitions with 65% and 34% weights, respectively. Similar NTOs structure and transitions weights are obtained in all four XC functionals and basis sets.

Initial conditions for MCE-AIMC simulations were obtained from previous equilibrated ground state DFT-MD at 300 K performed during 70 ps. These simulations were started from their corresponding optimized geometries using different XC functionals and basis sets. Ten atomic unit ( $\sim 0.24$  fs) nuclear time steps were used for these simulations. A stochastic velocity rescaling thermostat was applied to achieve the canonical ensemble.<sup>5</sup> The current AIMC algorithm is based on the conformational sampling approximation,<sup>17</sup> which means that only the nuclear overlap between cloned trajectories is considered. This is because cloned trajectories start from the

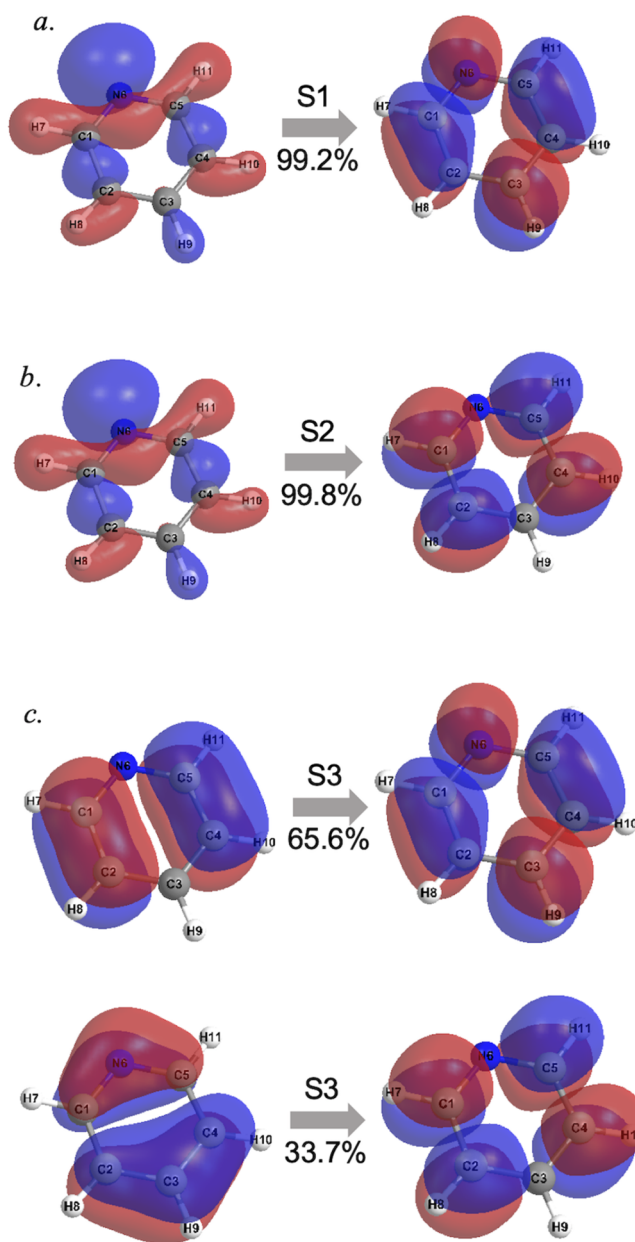


**Figure 1.** Natural transition orbitals (NTOs) plot for the (a)  $S_1$  ( $n - \pi^*$ ), (b)  $S_2$  ( $n - \pi^*$ ), and (c)  $S_3$  ( $\pi - \pi^*$ ). The corresponding weight for each NTO pair is shown under the arrow. All excitations are evaluated at the ground-state optimal geometry.

same initial conditions. In other words, the nuclear overlaps  $\langle \chi_m | \chi_n \rangle$ , where  $m$  and  $n$  are configurations, are practically zero (or uncorrelated) between initial independent configurations obtained from sufficiently large equilibrated ground state sampling. To achieve this conformational sampling, the initial configurations drawn from the ground state MD should be as diverse as possible. Accordingly, after an initial 10 ps of equilibration (with self-consistent field, SCF, convergence thresholds set to  $10^{-8}$  hartrees), initial conditions were obtained from 60 equally spaced-in-time snapshots collected during the subsequent 60 ps of the corresponded equilibrated ground state dynamics at room temperature. A detailed analysis of AIMC convergence related to the initial conformational sampling and parameter settings can be found elsewhere.<sup>69</sup>

Following the NTOs analysis, all MCE-AIMC runs were initiated on the bright  $S_3$  excited state. Typically, the excited state populations decay unidirectionally to the lower states from the initial state. However, to account for nonvanishing upward transitions, more states need to be included into simulations. As such, we use four excited states ( $S_1, \dots, S_4$ ) in the AIMC propagation, and all excited states were computed within LR-TDDFT/TDA. For each trajectory, 1 au ( $\sim 0.024$  fs) is used for nuclear time step, and the electronic time step is set to  $1/100$  au ( $\sim 2.4 \times 10^{-4}$  fs). An analysis of the numerical error in the MCE calculation related to time step setting is given in SI. Usually, a time step around 1–10 au and  $\Delta t = 10\text{--}100 \delta t$  is sufficient to maintain the numerical error in a acceptable range (see a discussion for Figure 2 b). In total, the

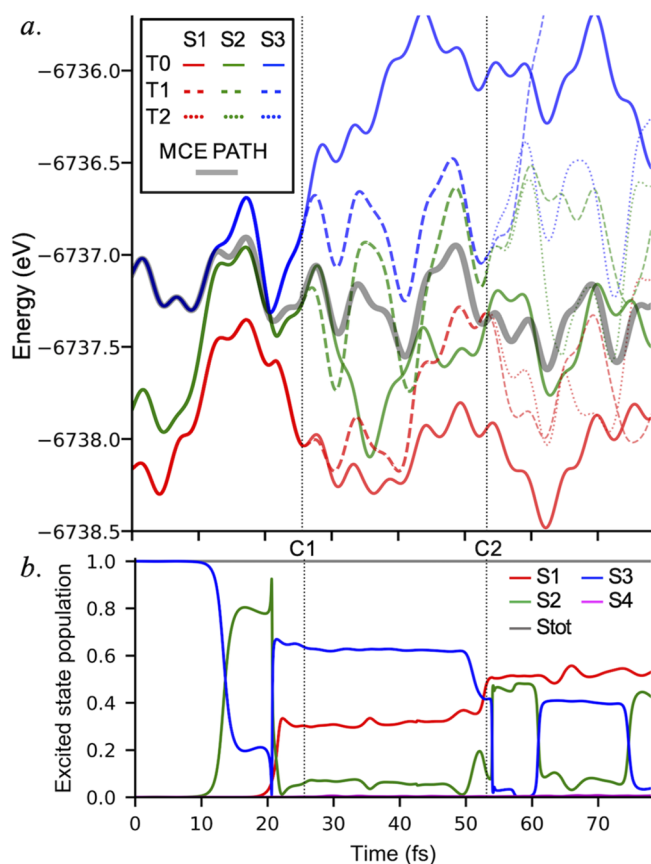


**Figure 2.** Trajectory example illustrating the internal conversion of  $S_3$  to  $S_1$  over 80 fs calculated using PBE0/Def2-SVP approach. The single initial trajectory experiences two cloning events at times C1 and C2, and splits into 3 trajectories. (a) Plots of the time evolution of the energies of  $S_3$ ,  $S_2$ , and  $S_1$  states for each TBF. The dark solid line shows the expected MCE path from all TBFs. (b) Plots of the excited state population calculated in AIMC simulation. The gray line is the sum of populations across all MCE states.

AIMC propagation was started with 60 independent Ehrenfest TBFs for 100 fs, which were gradually expanded to 250–280 TBFs as a result of cloning. A sample of the input file for MCE-AIMC simulation of pyridine molecule is given in the Supporting Information. The following MCE-AIMC results are focused on the def2-SVP basis sets. The result from the minimal STO-3G basis sets are listed in SI as for comparison.

Internal conversion in molecules involving excited electronic states typically occurs on time scales below  $\sim 1$  ps. Non-radiative and radiative transitions to the ground state usually

takes much longer (nanosecond) time scales. Hereafter, we focus on dynamics spanning the  $S_1, \dots, S_4$  excited state manifold. Notably, as mentioned in other published works,<sup>29,90</sup> conical intersections between the ground state and an excited state have incorrect dimensionality with LR-TDDFT<sup>91</sup> because of Brillouin's theorem.<sup>92</sup> This calls for the use of alternative approaches.<sup>31,85,93–95</sup>

Figure 2a and b show state energies and excited state population, respectively, of a typical trajectory from an AIMC simulation. Here, a single initial trajectory underwent two cloning events and is ultimately split into 3 trajectories. At the time C1, the PES of the two most populated states,  $S_3$  and  $S_1$ , significantly diverge from each other, which leads to a breakdown of the mean-field EHR. In such a case, the cloning algorithm is triggered to expand the original TBF (T0) with a new trajectory (T1) starting purely on  $S_3$  state, while the original T0 trajectory collects the TBF contributions of all other electronic states. A similar cloning event can be observed at time C2 between  $S_3$  and  $S_1$  states for a trajectory T1. Calculated expected MCE potential energy (eq 35) is then shown by the dark solid line in Figure 2a. It is clear that the expected potential energy path follows gradual population decay, converting from the pure  $S_3$  state to a MCE average of  $S_2$  and  $S_1$ . The continuity of the expected potential path at each cloning moments indicates excellent conservation of potential energy in the MCE framework.

The MCE basis sets are particularly advantageous when the electronic nonadiabatic coupling is strong. As shown in Figure 2b, the frequent electronic transitions around 10–22 and 53–75 fs indicates the presence of the conical intersection seam between  $S_3$  and  $S_2$ . Meanwhile, the cloning events increase the decoherent process and damp the rapid oscillation of the cloned state ( $S_3$  at time C1 and  $S_1$  at time C2). Notably, the cloning process does not prevent the cloned state from either being involved in a new coupling later or does it affect the coupling with the other states. The gray line in Figure 2b shows the sum of the state population in multiconfiguration, which is the norm of the MCE wave function (eq 12). Numerical errors can arise in the MCE calculations due to the rapidly changing Ehrenfest amplitudes  $a_i^{(n)}$ , especially in the strong nonadiabatic coupling regions. They can be reduced by narrowing both of the nuclear and electronic time step (see SI section I) or restricting the cloning frequency, which are discussed in the following section. In the current study, a 1% deviation limit is imposed for the norm (i.e., 0.99–1.01) to ensure conservation in the MCE calculation.

As described in section 2.3, the AIMC approach is based on three cloning criteria. criteria 1 (eq 26) and 2 (eq 27) are designed to ensure meaningful nuclear motion with Ehrenfest TBFs. Both criteria efficiently facilitate TBFs to explore the dynamically important regions of the conformational space. While the third criterion is not strictly necessary, it has been mainly proposed to control the rate of basis set growth. The cloning process offers to fix the EHR failures when the PES of populated electronic states significantly diverge. Therefore, too few cloning events will limit the AIMC benefits compared to EHR/MCE.<sup>45,46</sup> On the other hand, each cloning event adds a new trajectory in the simulation. Because of the parallel execution of the original and cloned trajectories, the overall computational loading is then increased proportionally by cloning, which may significantly slow down the progress of the simulation. Moreover, as mentioned above, the numerical error in MCE calculations accumulates as cloning increases.

Consequently, selecting an effective criterion 3 to control the cloning frequency in a reasonable range, is essential to the AIMC efficiency.

The original criterion 3 by Freixas et al.,<sup>45</sup> depends on the NACR vectors, which can be very jagged, so it has been modified for consistency with respect to the previous formulation. However, this modification has vanishing impact on the results since it only differentiates strong and weak coupling regimes, where differences are of several orders of magnitude. Based on our previous experience,<sup>45,46</sup> an AIMC simulation with limit of less than three cloning events per initial trajectory does not show much difference from the EHR, but with more than 12 clonings does not provide any further improvement. Subsequently, we limit the maximum number of cloning events to 12, and a value  $\delta = 0.005$  is set for the criterion 3 (Eq. 28) based on our test runs with STO-3G basis set (See discussion in SI: Section 2).

Figure 3 shows further analysis of criterion 3 (Eq. 28) with  $\delta = 0.005$  for different XC functionals. During the initial 100 fs of

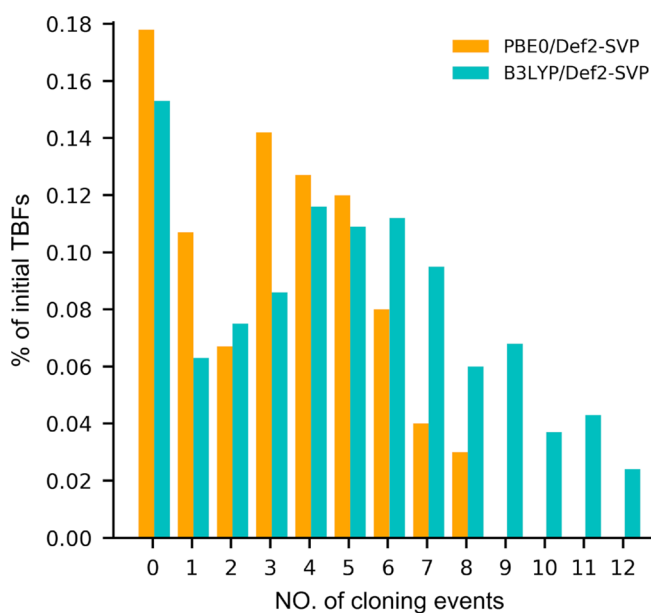


**Figure 3.** Distribution of cloning events per original TBFs for different functionals.

MCE-AIMC NAMD simulations, about 70% of the initial trajectories are cloned more than twice, and a significant peak can be observed for 3–5 cloning events in all methods. The results for B3LYP functional and both basis sets show a broad distribution of the clonings up to the limit. In contrast, the PBE0 results are centralized around 3 to 4 cloning times with no initial trajectories cloned by more than 8 times. These trends can be tentatively linked to effective gaps between excited states: larger gaps generally indicate smaller interactions between states. For DFT methodologies tested, we found that criterion 3 value should be between 0.002 to 0.05. Smaller  $\delta$  values ( $<0.002$ ) prevent cloning, whereas larger values ( $>0.05$ ) can introduce avalanching cloning events in regions of strong nonadiabatic coupling and cause an unnecessary increase in computational expense.

Figure 4 compares the time evolution of the average populations for the lowest three electronic excited states evaluated by MCE. Initially, oscillatory population exchange is observed between  $S_3$  and  $S_2$  states up to 80 fs of excitation

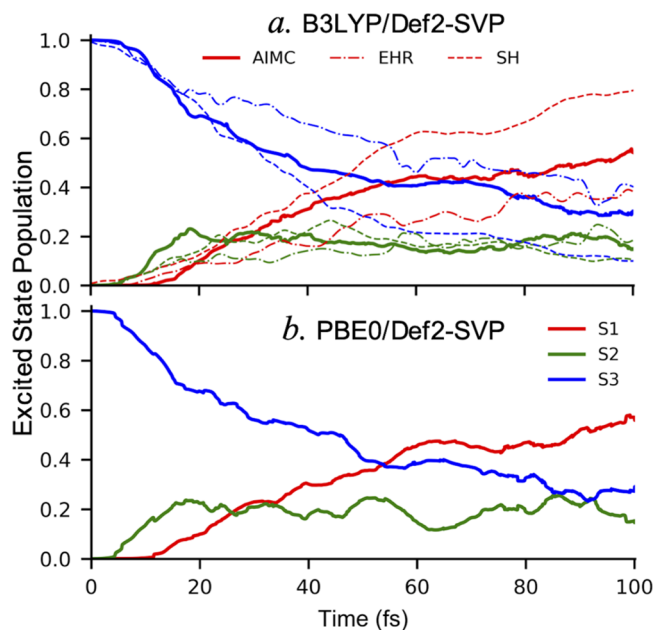


**Figure 4.** Time evolution of the excited state populations calculated (a) with B3LYP/Def2-SVP method and comparing between AIMC (solid lines), EHR (dashed-dotted lines), and SH (dashed lines) and (b) using PBE0/Def2-SVP method.

dynamics, particularly in B3LYP simulations. Such oscillations typically signify the presence of coherent electron-vibrational dynamics.<sup>7,45,46,51</sup> Both of the PBE0 and B3LYP results show similar  $S_3$  to  $S_1$  relaxation rates. To validate the new implemented AIMC and EHR methods, a comparison of the results with the existed SH method using decoherence correction in NWChem.<sup>32</sup> All three simulations are run in identical initial conditions with B3LYP/Def2-SVP setting. As shown in Figure 4a, SH method provides faster relaxation times as was also shown in the previous work.<sup>69</sup> Partially, this may be attributed to forbidden hops in SH that prevent expected populations transfer to higher energy states (e.g.,  $S_3 \rightarrow S_4$ ) introducing internal inconsistencies to the method. The use of ad hoc decoherence corrections overcome this deficiency, leading to the depletion of the quantum amplitudes in high energy states. Notably, by construction, AIMC trajectories explore larger areas of configurational space than EHR simulations. Cloning events improve the sampling of phase space regions dominated by relaxation pathways involving state-specific vibrational fluxes that are not explored by EHR simulations and allows for natural decoherence through wave function phase-space separation. Thus, AIMC results are mostly free from artifacts imposed by a mean field dynamics. In this sense, AIMC manages to capture aspects of the nuclear dynamics covered by SH simulations at a quantitative level, particularly once the states are no longer coupled. Besides, AIMC naturally incorporates electronic decoherence, leading to faster relaxations than EHR, but slower than SH simulations.<sup>45,46,69</sup>

Nuclear motion on the higher excited state typically leads the TBF close to regions of the configuration space with strong nonadiabatic coupling.<sup>96,97</sup> Therefore, this is an expected effect in the cloning procedure and, as in surface-hopping, it highlights electronic state-specific nuclear motions. Notably, the MCE-AIMC method naturally includes the upward wavepacket motion, leading to populations oscillations. With

built in decoherent mechanism through cloning, AIMC retains the effect of nuclear motions in the specific excited states for long times. In this way, the motions on the  $S_2$  state can lead to regions of the conformational space with a smaller energy gap between the  $S_3$  and  $S_2$  states. This induces more efficient coupling between both surfaces. Finally, it is notable that the use of cloning reduces the residual populations of higher-energy states (in the current case  $S > 3$ ). As shown in Figure 2b, the maximum  $S_4$  population is less than 0.01 in all MCE-AIMC simulations. These higher-energy states contribute with weak quasi-random fluctuations of the Ehrenfest force, which contributes to decoherence as well.<sup>36</sup> The effect of TBF cloning on the coherence will be further analyzed in future studies.

The nitrogen atom in the pyridine molecule breaks the symmetry of the perfect ring structure (e.g., like in the benzene). Figure 5a shows the orbital representation of state transition densities of pyridine at the ground-state optimal geometry. While the  $S_3$  state is nearly uniformly distributed across the ring, the  $S_2$  state tends to localize on the nitrogen side, and finally, the  $S_1$  state is centered on the nitrogen atom. This is suggestive that the internal conversion in the pyridine is followed by a unidirectional energy transfer from carbon atoms

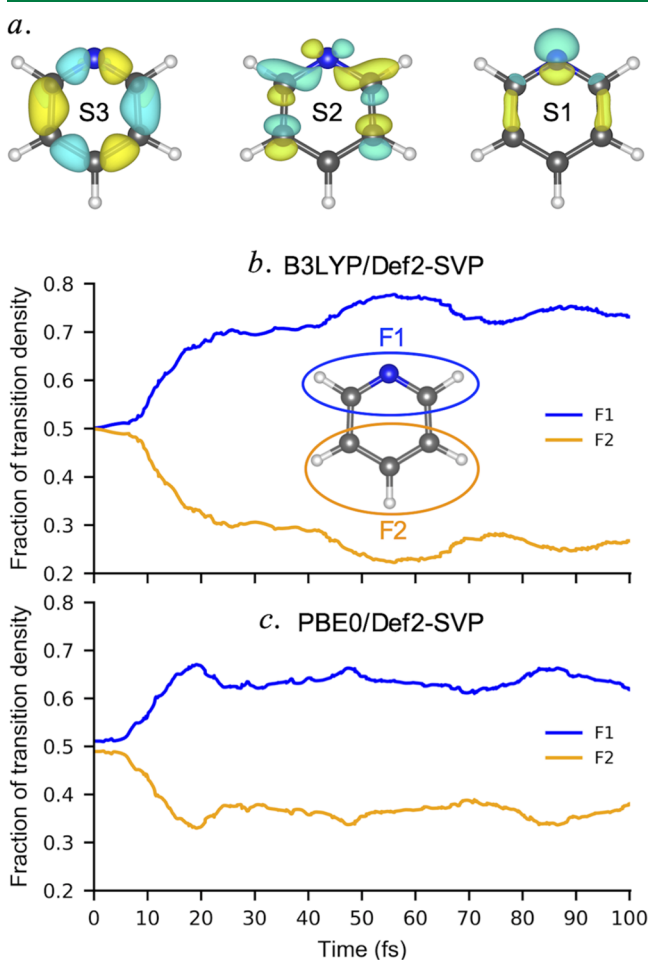


**Figure 5.** Transition density analysis of pyridine molecule. (a) Orbital plot of the transition density for the  $S_3$ ,  $S_2$ , and  $S_1$  electronic states at the ground-state optimal geometry. Time evolution plots of the transition density fractions localized on the F1 (with N atom) and F2 (without N atom) part obtained from MCE-AIMC simulations with (b) B3LYP/Def2-SVP and (c) PBE0/Def2-SVP methods.

to nitrogen. According to that, the transition density is separated into two fractions on the ring, with one fraction (F1) containing the nitrogen, and the other fraction (F2) encompassing carbons on the opposite side of the ring as shown in the inset of Figure 5b. Figure 5b and c shows the time evolution of these two transition densities partitioned into these fractions ( $\langle \hat{\rho}_X \rangle$ ) calculated by eq 39. Concomitant to the excited state populations (Figure 4) profile, a rapidly oscillating F2 to F1 transition density shift is observed in the range of  $\sim 10$ – $20$  fs following  $S_3$  to  $S_2$  population transfer. The B3LYP/Def2-SVP result has a higher F1 ratio and shows a higher electron transition rate with a long time oscillatory behavior up to 100 fs. In contrast, the PBE0/Def2-SVP method holds a relatively lower transition density fraction in F1, which saturates after the initial peak around 20 fs. Combining with the cloning times distribution plot in Figure 3, the frequency of cloning events influences the decoherent rate, which in turn affects oscillatory evolution of the electronic transition density.

Intramolecular vibrational energy redistribution takes place concomitant to the electronic energy transfer. The nuclear motions play a critical role in the process and can be followed by monitoring the specific bond lengths. Figure 6 plots the

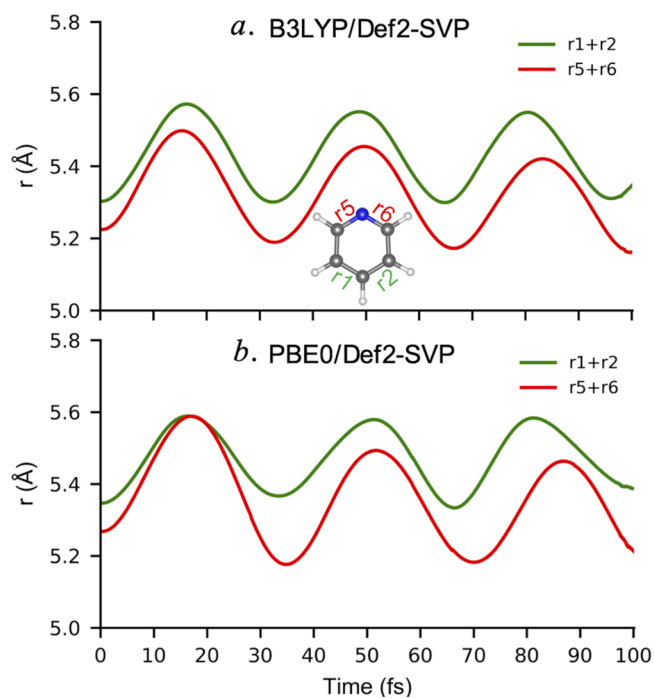


**Figure 6.** Average length of  $r_1 + r_2$  and  $r_5 + r_6$  bonds as a function of time obtained from MCE-AIMC simulations with (a) B3LYP/Def2-SVP and (b) PBE0/Def2-SVP methods.

bond length evolution of  $\langle \chi_n | \mathbf{R}^{(i)} | \chi_m \rangle$  calculated by eq 41 for the bonds on the nitrogen  $r_5 + r_6$  and the opposite  $r_1 + r_2$  sides. Both B3LYP/Def2-SVP and PBE0/Def2-SVP methods show excitation of bond-stretching motions initiated by excited state dynamics over the entire ring. In-phase evolution of bonds on the upper and lower parts of the ring suggests overall pyridine ring breathing excited by internal conversion.

Table 2 shows CPU times for each calculation in an MCE-AIMC time step of pyridine using the PBE0 functional and Def2-SVP basis set (109 basis functions). These timing tests were performed 36 CPUs computer node at LANL Institutional Computing facilities. There are 6 eigenstates considered

**Table 2. CPU Timings (in Units of Seconds) for a MCE-AIMC Timestep of Pyridine with PBE0/Def2-SVP<sup>a</sup>**

calculation	CPU times (s)
TDDFT energy	10.8
EHR gradient	72.9
MCE	0.1

<sup>a</sup>Tests were performed on a computer system with 36 Intel Xeon Processors E5-2695 v4 (45M Cache, 2.10 GHz).

in the TDDFT calculation, and the EHR gradient is mean-field averaged by the lowest 4 excited-state. All CPU times are averaged with respect to the time spent for one trajectory in an  $N$  ( $N > 1$ ) cloned multiconfiguration system. The cost of electronic structure and state energy calculation (DFT + TDDFT) is a proportionality constant growing sublinearly with the number of electronic states. The total number of states (1 ground-state +  $(n + 1)$  excited-states) in TDDFT energy calculation have to be larger than the number of states ( $n$ ) involved in Ehrenfest gradients calculation. The following mean-field Ehrenfest gradients calculation, which included TDDFT gradient in each excited-state, trivial crossing check, NACT, and NACR calculation, is the most time-consuming step. The MCE calculation with cloning evaluation only adding a minor cost at each nuclear step.

## 5. CONCLUSIONS

We have presented our implementation of the ab initio multiple cloning algorithm combined with the multiconfigurational Ehrenfest (MCE-AIMC) method in the NWChem computational chemistry program. Efficient calculation of state energies, gradients and nonadiabatic couplings at LR-TDDFT electronic structure level, allows for computing all observables on-the-fly and performing nonadiabatic excited state molecular dynamics simulations in multiatomic molecules on time scales of hundreds of femtoseconds, which are typical for internal conversion processes in organic chromophores. To demonstrate and validate our implementation, we have simulated the photoinduced dynamics in the pyridine using several DFT models and basis sets, and compared the NAMD results between the new implemented MCE-AIMC, EHR methods and the surface hopping method. The effects of the cloning procedure are examined in detail through the trajectory analysis, evolution of the excited state populations and induced vibrational motions coupled to the electronic dynamics. Overall, the calculated photoexcited dynamics of pyridine is qualitatively similar for different DFT methods used. We found that the MCE-AIMC approach describes the expected population exchange between electronic states reinforced by state specific nuclear motions. A particular strength of this methodology is its ability to describe coherent electron-vibrational dynamics as reflected in oscillations observed in the trajectories and other variables analyzed.

## ■ ASSOCIATED CONTENT

### Supporting Information

The Supporting Information is available free of charge at <https://pubs.acs.org/doi/10.1021/acs.jctc.1c00131>.

Discussion concerning numerical errors during MCE simulations related to classical and quantum time scales; MCE-AIMC results using different exchange-correlation functionals and basis sets; examples of NWChem input

and MCE observable calculation input files; and pyridine ground-state optimized structure (PDF)

## ■ AUTHOR INFORMATION

### Corresponding Authors

**Huajing Song** – *Physics and Chemistry of Materials, Theoretical Division, Los Alamos National Laboratory, Los Alamos, New Mexico 87545, United States*; [orcid.org/0000-0001-5958-7377](https://orcid.org/0000-0001-5958-7377); Email: [songhw@lanl.gov](mailto:songhw@lanl.gov)

**Niranjan Govind** – *Physical and Computational Sciences Directorate, Pacific Northwest National Laboratory, Richland, Washington 99352, United States*; [orcid.org/0000-0003-3625-366X](https://orcid.org/0000-0003-3625-366X); Email: [niri.govind@pnnl.gov](mailto:niri.govind@pnnl.gov)

**Sergei Tretiak** – *Physics and Chemistry of Materials, Theoretical Division and Center for Integrated Nanotechnologies, Los Alamos National Laboratory, Los Alamos, New Mexico 87545, United States*; [orcid.org/0000-0001-5547-3647](https://orcid.org/0000-0001-5547-3647); Email: [serg@lanl.gov](mailto:serg@lanl.gov)

### Authors

**Victor M. Freixas** – *Departamento de Ciencia y Tecnologia, Universidad Nacional de Quilmes/CONICET, B1876BXD Bernal, Argentina*; [orcid.org/0000-0003-1733-4827](https://orcid.org/0000-0003-1733-4827)

**Sebastian Fernandez-Alberti** – *Departamento de Ciencia y Tecnologia, Universidad Nacional de Quilmes/CONICET, B1876BXD Bernal, Argentina*; [orcid.org/0000-0002-0916-5069](https://orcid.org/0000-0002-0916-5069)

**Alexander J. White** – *Physics and Chemistry of Materials, Theoretical Division, Los Alamos National Laboratory, Los Alamos, New Mexico 87545, United States*

**Yu Zhang** – *Physics and Chemistry of Materials, Theoretical Division, Los Alamos National Laboratory, Los Alamos, New Mexico 87545, United States*; [orcid.org/0000-0001-8938-1927](https://orcid.org/0000-0001-8938-1927)

**Shaul Mukamel** – *Departments of Chemistry, Physics, and Astronomy, University of California, Irvine, California 92697, United States*; [orcid.org/0000-0002-6015-3135](https://orcid.org/0000-0002-6015-3135)

Complete contact information is available at: <https://pubs.acs.org/doi/10.1021/acs.jctc.1c00131>

### Notes

The authors declare no competing financial interest.

## ■ ACKNOWLEDGMENTS

H.S., S.T., N.G., and S.M. acknowledge support from the U.S. Department of Energy, Office of Science, Basic Energy Sciences, Chemical Sciences, Geosciences, and Biosciences Division under Contracts No. KC0301030, KC030103172684, and award No. DE-SC0019484. S.T. acknowledges support of the Center for Integrated Nanotechnology (CINT) at Los Alamos National Laboratory (LANL), a U.S. Department of Energy and Office of Basic Energy Sciences User Facility. V.M.F and S.F.A. acknowledge partial support from CONICET, UNQ, ANPCyT (PICT-2018-2360). This research used resources provided by the LANL Institutional Computing Program and also benefited from computational resources provided by EMSL, a DOE Office of Science User Facility sponsored by the Office of Biological and Environmental Research and located at the Pacific Northwest National Laboratory (PNNL). PNNL is operated by Battelle Memorial Institute for the United States Department of Energy under DOE contract number DE-AC05-76RL1830.

## REFERENCES

- (1) Yarkony, D. R. Diaboloical conical intersections. *Rev. Mod. Phys.* **1996**, *68*, 985.
- (2) Domcke, W.; Yarkony, D. R. Role of Conical Intersections in Molecular Spectroscopy and Photoinduced Chemical Dynamics. *Annu. Rev. Phys. Chem.* **2012**, *63*, 325–352.
- (3) Baer, M. *Beyond Born-Oppenheimer: Electronic Nonadiabatic Coupling Terms and Conical Intersections*; John Wiley & Sons, 2006.
- (4) Mai, S.; González, L. Unconventional two-step spin relaxation dynamics of [Re(CO)<sub>3</sub>(im)(phen)]<sup>+</sup> in aqueous solution. *Chem. Sci.* **2019**, *10*, 10405–10411.
- (5) Nelson, T.; Fernandez-Alberti, S.; Chernyak, V.; Roitberg, A.; Tretiak, S. Nonadiabatic Excited-State Molecular Dynamics Modeling of Photoinduced Dynamics in Conjugated Molecules. *J. Phys. Chem. B* **2011**, *115*, 5402–5414.
- (6) Kossoski, F.; Varella, M. T. d. N.; Barbatti, M. On-the-fly dynamics simulations of transient anions. *J. Chem. Phys.* **2019**, *151*, 224104.
- (7) Nelson, T.; Ondarse-Alvarez, D.; Oldani, N.; Rodriguez-Hernandez, B.; Alfonso-Hernandez, L.; Galindo, F. J.; Kleiman, D. V.; Fernandez-Alberti, S.; Roitberg, A.; Tretiak, S. Coherent exciton-vibrational dynamics and energy transfer in conjugated organics. *Nat. Commun.* **2018**, *9*, 2316.
- (8) Abiola, T. T.; Rodrigues, N. d. N.; Ho, C.; Coxon, D. J. L.; Horbury, M. D.; Toldo, J. M.; do Casal, M. T.; Rioux, B.; Peyrot, C.; Mention, M. M.; Balaguer, P.; Barbatti, M.; Allais, F.; Stavros, V. G. New Generation UV-A Filters: Understanding Their Photodynamics on a Human Skin Mimic. *J. Phys. Chem. Lett.* **2021**, *12*, 337–344.
- (9) Nelson, T.; Fernandez-Alberti, S.; Roitberg, A.; Tretiak, S. Nonadiabatic Excited-State Molecular Dynamics: Modeling Photo-physics in Organic Conjugated Materials. *Acc. Chem. Res.* **2014**, *47*, 1155–1164.
- (10) Jailaubekov, A. E.; Willard, A. P.; Tritsch, J. R.; Chan, W.-L.; Sai, N.; Gearba, R.; Kaake, L. G.; Williams, K. J.; Leung, K.; Rossky, P. J.; Zhu, X.-Y. Hot Charge-Transfer Excitons Set the Time Limit for Charge Separation at Donor/Acceptor Interfaces in Organic Photovoltaics. *Nat. Mater.* **2013**, *12*, 66–73.
- (11) Soler, A. M.; Nelson, T.; Roitberg, A.; Tretiak, S.; Fernandez-Alberti, S. Signature of Nonadiabatic Coupling in Excited-State Vibrational Modes. *J. Phys. Chem. A* **2014**, *118*, 10372–10379.
- (12) Yu, J. K.; Bannwarth, C.; Liang, R.; Hohenstein, E. G.; Martínez, T. J. Nonadiabatic Dynamics Simulation of the Wavelength-Dependent Photochemistry of Azobenzene Excited to the  $n\pi^*$  and  $\pi\pi^*$  Excited States. *J. Am. Chem. Soc.* **2020**, *142*, 20680–20690.
- (13) Nelson, T.; Fernandez-Alberti, S.; Roitberg, A.; Tretiak, S. Electronic Delocalization, Vibrational Dynamics, and Energy Transfer in Organic Chromophores. *J. Phys. Chem. Lett.* **2017**, *8*, 3020–31.
- (14) Crespo-Otero, R.; Barbatti, M. Recent Advances and Perspectives on Nonadiabatic Mixed Quantum-Classical Dynamics. *Chem. Rev.* **2018**, *118*, 7026–7068.
- (15) Nelson, T.; White, J. A.; Bjorgaard, A. J.; Sifain, E. A.; Zhang, Y.; Nebgen, B.; Fernandez-Alberti, S.; Mozyrsky, D.; Roitberg, A.; Tretiak, S. Non-adiabatic Excited State Molecular Dynamics: theory and applications for modeling photophysics in extended molecular materials. *Chem. Rev.* **2020**, *120*, 2215–2287.
- (16) González, L.; Lindh, R. *Quantum Chemistry and Dynamics of Excited States: Methods and Applications*; Wiley, 2020.
- (17) Makhov, D. V.; Glover, W. J.; Martinez, T. J.; Shalashilin, D. V. Ab initio multiple cloning algorithm for quantum nonadiabatic molecular dynamics. *J. Chem. Phys.* **2014**, *141*, 054110.
- (18) Billing, G. D. On the use of Ehrenfest's theorem in molecular scattering. *Chem. Phys. Lett.* **1983**, *100*, 535–9.
- (19) Tully, J. C. Molecular Dynamics with Electronic Transitions. *J. Chem. Phys.* **1990**, *93*, 1061–1071.
- (20) Neukirch, A. J.; Shamberger, L. C.; Abad, E.; Haycock, B. J.; Wang, H.; Ortega, J.; Prezhdo, O. V.; Lewis, J. P. Nonadiabatic ensemble simulations of cis-stilbene and cis-azobenzene photo-isomerization. *J. Chem. Theory Comput.* **2014**, *10*, 14–23.
- (21) Subotnik, J. E.; Shenvi, N. A new approach to decoherence and momentum rescaling in the surface hopping algorithm. *J. Chem. Phys.* **2011**, *134*, 024105.
- (22) Akimov, A.; Smith, B.; Sato, K.; Li, W.; Sun, X.; Chan, M. Quantum-Dynamics-Hub/libra-code: First Official Indexed Release. Zenodo, 2019. <https://zenodo.org/record/3594534#.YJvWu7VKiyI>.
- (23) Richter, M.; Marquetand, P.; González-Vázquez, J.; Sola, I.; González, L. SHARC: Ab Initio Molecular Dynamics with Surface Hopping in the Adiabatic Representation Including Arbitrary Couplings. *J. Chem. Theory Comput.* **2011**, *7*, 1253–1258.
- (24) Hammes-Schiffer, S. Hydrogen tunneling and protein motion in enzyme reactions. *Acc. Chem. Res.* **2006**, *39*, 93–100.
- (25) Antol, I.; Eckert-Maksic, M.; Barbatti, M.; Lischka, H. Simulation of the photodeactivation of formamide in the  $n\sigma-\pi^*$  and  $\pi-\pi^*$  states: An ab initio on-the-fly surface-hopping dynamic study. *J. Chem. Phys.* **2007**, *127*, 234303.
- (26) Prezhdo, O. V. Photoinduced dynamics in semiconductor quantum dots: insights from time-domain ab initio studies. *Acc. Chem. Res.* **2009**, *42*, 2005–2016.
- (27) Malone, W.; Nebgen, B.; White, A.; Zhang, Y.; Song, H.; Bjorgaard, J.; Sifain, A.; Rodriguez-Hernandez, B.; Freixas, V.; Fernandez-Alberti, S.; Roitberg, E.; Nelson, R.; Tretiak, S. NEXMD Software Package for Non-adiabatic Excited State Molecular Dynamics Simulations. *J. Chem. Theory Comput.* **2020**, *16*, 5771.
- (28) Balasubramani, S. G.; Chen, G. P.; Coriani, S.; Diederhofen, M.; Frank, M. S.; Franzke, Y. J.; Furche, F.; Grotjahn, R.; Harding, M. E.; Hättig, C.; Hellweg, A.; Helmich-Paris, B.; Holzer, C.; Huniar, U.; Kaupp, M.; Marefat Khah, A.; Karbalaeei Khani, S.; Müller, T.; Mack, F.; Nguyen, B. D.; Parker, S. M.; Perlt, E.; Rappoport, D.; Reiter, K.; Roy, S.; Rückert, M.; Schmitz, G.; Sierka, M.; Tapavicza, E.; Tew, D. P.; van Wüllen, C.; Voora, V. K.; Weigend, F.; Wodyński, A.; Yu, J. M. TURBOMOLE: Modular program suite for ab initio quantum-chemical and condensed-matter simulations. *J. Chem. Phys.* **2020**, *152*, 184107.
- (29) Parker, S.; Roy, S.; Furche, F. Multistate hybrid time-dependent density functional theory with surface hopping accurately captures ultrafast thymine photodeactivation. *Phys. Chem. Chem. Phys.* **2019**, *21*, 18999–19010.
- (30) Ryabinkin, I.; Nagesh, J.; Izmaylov, F. Fast Numerical Evaluation of time-Derivative Nonadiabatic Couplings for Mixed Quantum-Classical Methods. *J. Phys. Chem. Lett.* **2015**, *6*, 4200–4203.
- (31) Zhang, Y.; Li, L.; Tretiak, S.; Nelson, T. R. Non-Adiabatic Excited-State Molecular Dynamics for Open-Shell Systems. *J. Chem. Theory Comput.* **2020**, *16*, 2053–64.
- (32) Song, H.; Fischer, S. A.; Zhang, Y.; Cramer, C. J.; Mukamel, S.; Govind, N.; Tretiak, S. First Principles Nonadiabatic Excited-State Molecular Dynamics in NWChem. *J. Chem. Theory Comput.* **2020**, *16*, 6418.
- (33) Makhov, D. V.; Symonds, C.; Fernandez-Alberti, S.; Shalashilin, D. V. Ab initio quantum direct dynamics simulations of ultrafast photochemistry with multiconfigurational Ehrenfest approach. *Chem. Phys.* **2017**, *493*, 200–18.
- (34) Shalashilin, D. V. Nonadiabatic dynamics with the help of multiconfigurational Ehrenfest method: Improved theory and fully quantum 24D simulation of pyrazine. *J. Chem. Phys.* **2010**, *132*, 244111–7334.
- (35) Saita, K.; Shalashilin, D. V. On-the-fly ab initio molecular dynamics with multiconfigurational Ehrenfest method. *J. Chem. Phys.* **2012**, *137*, 22A506–7334.
- (36) Fernandez-Alberti, S.; Makhov, D. V.; Tretiak, S.; Shalashilin, D. V. Non-adiabatic excited state molecular dynamics of phenylene ethynylene dendrimer using a multiconfigurational Ehrenfest approach. *Phys. Chem. Chem. Phys.* **2016**, *18*, 10028–40.
- (37) Richings, G.; Polyak, I.; Spinlove, K.; Worth, G.; Burghardt, I.; Lasorne, B. Quantum dynamics simulations using Gaussian wave-packets: the vMCG method. *Int. Rev. Phys. Chem.* **2015**, *34*, 269–308.
- (38) Mendive-Tapia, D.; Lasorne, B.; Worth, G. A.; Bearpark, M. J.; Robb, M. A. Controlling the mechanism of fulvene S(1)/S(0) decay:

switching off the stepwise population transfer. *Phys. Chem. Chem. Phys.* **2010**, *12*, 15725–15733.

(39) Ben-Nun, M.; Martínez, T. J. *Advances in Chemical Physics*; John Wiley & Sons, Ltd., 2002; pp 439–512.

(40) Ben-Nun, M.; Quenneville, J.; Martínez, T. J. Ab Initio Multiple Spawning: Photochemistry from First Principles Quantum Molecular Dynamics. *J. Phys. Chem. A* **2000**, *104*, 5161–5175.

(41) Curchod, B. F. E.; Sisto, A.; Martínez, T. J. Ab Initio Multiple Spawning Photochemical Dynamics of DMABN Using GPUs. *J. Phys. Chem. A* **2017**, *121*, 265–276.

(42) Bera, A.; Ghosh, J.; Bhattacharya, A. Ab initio multiple spawning dynamics study of dimethylnitramine and dimethylnitramine-Fe complex to model their ultrafast nonadiabatic chemistry. *J. Chem. Phys.* **2017**, *147*, 044308.

(43) Makhov, D. V.; Saita, K.; Martínez, T. J.; Shalashilin, D. V. Ab initio multiple cloning simulations of pyrrole photodissociation: TKER spectra and velocity map imaging. *Phys. Chem. Chem. Phys.* **2015**, *17*, 3316–25.

(44) Makhov, D. V.; Martínez, T. J.; Shalashilin, D. V. Toward fully quantum modelling of ultrafast photodissociation imaging experiments. Treating tunnelling in the ab initio multiple cloning approach. *Faraday Discuss.* **2016**, *194*, 81–94.

(45) Freixas, V. M.; Fernandez-Alberti, S.; Makhov, D. V.; Tretiak, S.; Shalashilin, D. An ab initio multiple cloning approach for the simulation of photoinduced dynamics in conjugated molecules. *Phys. Chem. Chem. Phys.* **2018**, *20*, 17762–72.

(46) Freixas, V. M.; Tretiak, S.; Makhov, D. V.; Shalashilin, D. V.; Fernandez-Alberti, S. Vibronic Quantum Beating between Electronic Excited States in a Heterodimer. *J. Phys. Chem. B* **2020**, *124*, 3992–4001.

(47) Nelson, T.; Fernandez-Alberti, S.; Roitberg, A. E.; Tretiak, S. Artifacts due to trivial unavoided crossings in the modeling of photoinduced energy transfer dynamics in extended conjugated molecules. *Chem. Phys. Lett.* **2013**, *590*, 208–231.

(48) Fernandez-Alberti, S.; Roitberg, A. E.; Nelson, T.; Tretiak, S. Identification of unavoided crossings in nonadiabatic photoexcited dynamics involving multiple electronic states in polyatomic conjugated molecules. *J. Chem. Phys.* **2012**, *137*, 014512.

(49) Worth, G. A.; Robb, M. A.; Burghardt, I. A novel algorithm for non-adiabatic direct dynamics using variational Gaussian wavepackets. *Faraday Discuss.* **2004**, *127*, 307–323.

(50) Alfonso-Hernandez, L.; Nelson, R.; Gelin, M.; Lupton, J. M.; Tretiak, S.; Fernandez-Alberti, S. Interference of Interchromophoric Energy-Transfer Pathways in  $\pi$ -Conjugated Macrocycles. *J. Phys. Chem. Lett.* **2016**, *7*, 4936–44.

(51) Keefer, D.; Freixas, V. M.; Song, H.; Tretiak, S.; Fernandez-Alberti, S.; Mukamel, S. Probing Intramolecular Vibronic Coherences in Complex Molecules by Ultrafast Stimulated X-ray Raman Signals. *Chem. Sci.* **2021**, *12*, 5286–5294.

(52) Tretiak, S.; Zhang, W. M.; Chernyak, V.; Mukamel, S. Excitonic couplings and electronic coherence in bridged naphthalene dimers. *Proc. Natl. Acad. Sci. U. S. A.* **1999**, *96*, 13003–8.

(53) Mukamel, S.; Tretiak, S.; Wagersreiter, T.; Chernyak, V. Electronic Coherence and Collective Optical Excitations of Conjugated Molecules. *Science* **1997**, *277*, 781–7.

(54) Freixas, V. M.; Ondarse-Alvarez, D.; Tretiak, S.; Makhov, D. V.; Shalashilin, D. V.; Fernandez-Alberti, S. Photoinduced non-adiabatic energy transfer pathways in dendrimer building blocks. *J. Chem. Phys.* **2019**, *150*, 124301.

(55) Valiev, M.; Bylaska, E. J.; Govind, N.; Kowalski, K.; Straatsma, T. P.; van Dam, H. J. J.; Wang, D.; Nieplocha, J.; Apra, E.; Windus, T. L.; de Jong, W. A. NWChem: A Comprehensive and Scalable Open-Source Solution for Large Scale Molecular Simulations. *Comput. Phys. Commun.* **2010**, *181*, 1477–1489.

(56) Apra, E.; Bylaska, E. J.; De Jong, W. A.; Govind, N.; Kowalski, K.; Straatsma, T. P.; Valiev, M.; van Dam, H.; Alexeev, Y.; Anchell, J.; et al. NWChem: Past, present, and future. *J. Chem. Phys.* **2020**, *152*, 184102.

(57) Furche, F.; Ahlrichs, R. Adiabatic Time-Dependent Density Functional Methods for Excited State Properties. *J. Chem. Phys.* **2002**, *117*, 7433–7447.

(58) Casida, M. E.; Huix-Rotllant, M. Progress in time-dependent density-functional theory. *Annu. Rev. Phys. Chem.* **2012**, *63*, 287–323.

(59) Baer, R. Non-adiabatic couplings by time-dependent density functional theory. *Chem. Phys. Lett.* **2002**, *364*, 75–79.

(60) Baer, R.; Kurzweil, Y.; Cederbaum, L. S. Time-dependent density functional theory for nonadiabatic processes. *Isr. J. Chem.* **2005**, *45*, 161–170.

(61) Gross, E. K. U.; Dobson, J. F.; Petersilka, M. *Density Functional Theory II*; Springer-Verlag: Berlin, 1996; pp 81–172.

(62) Ullrich, C. A. *Time-Dependent Density-Functional Theory: Concepts and Applications*; Oxford University Press: Oxford, 2011.

(63) Silverstein, D. W.; Govind, N.; Van Dam, H. J.; Jensen, L. Simulating one-photon absorption and resonance Raman scattering spectra using analytical excited state energy gradients within time-dependent density functional theory. *J. Chem. Theory Comput.* **2013**, *9*, 5490–5503.

(64) Shalashilin, D. V.; Child, M. S. The phase space CCS approach to quantum and semiclassical molecular dynamics for high-dimensional systems. *Chem. Phys.* **2004**, *304*, 103–120.

(65) Thompson, A. L.; Punwong, C.; Martínez, T. J. Optimization of width parameters for quantum dynamics with frozen Gaussian basis sets. *Chem. Phys.* **2010**, *370*, 70–77.

(66) Fidler, A. F.; Singh, V. P.; Long, P. D.; Dahlberg, P. D.; Engel, G. S. Dynamic localization of electronic excitation in photosynthetic complexes revealed with chiral two-dimensional spectroscopy. *Nat. Commun.* **2014**, *5*, 3286.

(67) Berry, M. V. Quantal phase factors accompanying adiabatic changes. *Proc. R. Soc. London, Ser. A* **1984**, *392*, 45–57.

(68) Mead, C. A.; Truhlar, D. G. On the determination of Born-Oppenheimer nuclear motion wave functions including complications due to conical intersections and identical nuclei. *J. Chem. Phys.* **1979**, *70*, 2284–96.

(69) Freixas, V. M.; White, A. J.; Nelson, T.; Song, H.; Makhov, D. V.; Shalashilin, D.; Fernandez-Alberti, S.; Tretiak, S. Nonadiabatic Excited-State Molecular Dynamics Methodologies: Comparison and Convergence. *J. Phys. Chem. Lett.* **2021**, *12*, 2970–2982.

(70) Hirata, S.; Head-Gordon, M. Time-dependent density functional theory within the Tamm-Dancoff approximation. *Chem. Phys. Lett.* **1999**, *314*, 291–291.

(71) Tretiak, S.; Mukamel, S. Density Matrix Analysis and Simulation of Electronic Excitations in Conjugated and Aggregated Molecules. *Chem. Rev.* **2002**, *102*, 3171–3212.

(72) Mewes, S. A.; Mewes, J. M.; Dreuw, A.; Plasser, F. Excitons in poly(para phenylene vinylene): a quantum-chemical perspective based on high-level *ab initio* calculations. *Phys. Chem. Chem. Phys.* **2016**, *18*, 2548–63.

(73) Hirata, S.; Head-Gordon, M. Time-dependent density functional theory for radicals: An improved description of excited states with substantial double excitation character. *Chem. Phys. Lett.* **1999**, *302*, 375–382.

(74) Fischer, S. A.; Ueltschi, T. W.; El-Khoury, P. Z.; Mifflin, A. L.; Hess, W. P.; Wang, H.-f.; Cramer, C. J.; Govind, N. Infrared and Raman Spectroscopy from Ab Initio Molecular Dynamics and Static Normal Mode Analysis: The CH Region of DMSO as a Case Study. *J. Phys. Chem. B* **2016**, *120*, 1429.

(75) Ou, Q.; Bellchambers, G. D.; Furche, F.; Subotnik, J. E. First-Order Derivative Couplings between Excited States from Adiabatic TDDFT Response Theory. *J. Chem. Phys.* **2015**, *142*, 064114.

(76) Yaakub, A. R.; Evans, D. J. A fourth order Runge-Kutta RK(4,4) method with error control. *Int. J. Comput. Math.* **1999**, *71*, 383–411.

(77) Swope, W. C.; Andersen, H. C.; Berens, P. H.; Wilson, K. R. A Computer Simulation Method for the Calculation of Equilibrium Constants for the Formation of Physical Clusters of Molecules: Application to Small Water Clusters. *J. Chem. Phys.* **1982**, *76*, 637–649.

- (78) Tretiak, S.; Chernyak, V. Resonant nonlinear polarizabilities in the time-dependent density functional theory. *J. Chem. Phys.* **2003**, *119*, 8809–8823.
- (79) Bussi, G.; Donadio, D.; Parrinello, M. Canonical sampling through velocity rescaling. *J. Chem. Phys.* **2007**, *126*, 014101.
- (80) Adamo, C.; Barone, V. Toward reliable density functional methods without adjustable parameters: The PBE0 model. *J. Chem. Phys.* **1999**, *110*, 6158–6170.
- (81) Collins, J. B.; von R. Schleyer, P.; Binkley, J. S.; Pople, J. A. Self-Consistent Molecular Orbital Methods. 17. Geometries and binding energies of second-row molecules. A comparison of three basis sets. *J. Chem. Phys.* **1976**, *64*, 5142–5151.
- (82) Weigend, F.; Ahlrichs, R. Balanced Basis Sets of Split Valence, Triple Zeta Valence and Quadruple Zeta Valence Quality for H to Rn: Design and Assessment of Accuracy. *Phys. Chem. Chem. Phys.* **2005**, *7*, 3297–3305.
- (83) Becke, A. D. Density-functional thermochemistry. V. Systematic optimization of exchange-correlation functionals. *J. Chem. Phys.* **1997**, *107*, 8554–8561.
- (84) Peters, L. D. M.; Kussmann, J.; Ochsenfeld, C. Nonadiabatic Molecular Dynamics on Graphics Processing Units: Performance and Application to Rotary Molecular Motors. *J. Chem. Theory Comput.* **2019**, *15*, 6647–59.
- (85) Tapavicza, E.; Bellchambers, G. D.; Vincent, J. C.; Furche, F. *Ab Initio* non-adiabatic molecular dynamics. *Phys. Chem. Chem. Phys.* **2013**, *15*, 18336–18348.
- (86) Yu, H. S.; Li, S. L.; Truhlar, D. G. Perspective: Kohn-Sham density functional theory descending a staircase. *J. Chem. Phys.* **2016**, *145*, 130901.
- (87) Freixas, V. M.; Nelson, T.; Ondarse-Alvarez, D.; Nijjar, P.; Mikhailovsky, A.; Zhou, C.; Fernandez-Alberti, S.; Bazan, G. C.; Tretiak, S. Experimental and theoretical study of energy transfer in a chromophore triad: What makes modeling dynamics successful? *J. Chem. Phys.* **2020**, *153*, 244114.
- (88) Lorentzon, J.; Fülcher, M.; Roos, B. A theoretical study of the electronic spectra of pyridine and phosphabenzene. *Theoret. Chim. Acta* **1995**, *92*, 67–81.
- (89) Cai, Z.; Reimers, J. The Low-Lying Excited States of Pyridine. *J. Phys. Chem. A* **2000**, *104*, 8389–408.
- (90) Stojanović, L.; Bai, S.; Nagesh, J.; Izmaylov, A. F.; Crespo-Otero, R.; Lischka, H.; Barbatti, M. New Insights into the State Trapping of UV-Excited Thymine. *Molecules* **2016**, *21*, 1603.
- (91) Levine, B. G.; Ko, C.; Quenneville, J.; Martínez, T. J. Conical intersections and double excitations in time-dependent density functional theory. *Mol. Phys.* **2006**, *104*, 1039–1051.
- (92) Szabo, A.; Ostlund, N. S. *Modern Quantum Chemistry: Introduction to Advanced Electronic Structure Theory*; Courier Corporation, 2012.
- (93) Parker, S.; Rappoport, D.; Furche, F. Quadratic Response Properties from TDDFT: Trials and Tribulations. *J. Chem. Theory Comput.* **2018**, *14*, 807–819.
- (94) Li, S. L.; Marenich, A. V.; Xu, X.; Truhlar, D. G. Configuration Interaction-Corrected Tamm-Dancoff Approximation: A Time-Dependent Density Functional Method with the Correct Dimensionality of Conical Intersections. *J. Phys. Chem. Lett.* **2014**, *5*, 322–328.
- (95) Shu, Y.; Parker, K. A.; Truhlar, D. G. Dual-functional Tamm-Dancoff approximation: a convenient density functional method that correctly describes S1/S0 conical intersections. *J. Phys. Chem. Lett.* **2017**, *8*, 2107–2112.
- (96) Fernandez-Alberti, S.; Kleiman, V. D.; Tretiak, S.; Roitberg, A. E. Unidirectional Energy Transfer in Conjugated Molecules: The Crucial Role of High-Frequency C≡C Bonds. *J. Phys. Chem. Lett.* **2010**, *1*, 2699–704.
- (97) Fernandez-Alberti, S.; Roitberg, A. E.; Kleiman, V. D.; Nelson, T.; Tretiak, S. Shishiodoshi unidirectional energy transfer mechanism in phenylene ethynylene dendrimers. *J. Chem. Phys.* **2012**, *137*, 22A526.

# An *ab-initio* multiple cloning method for Non-Adiabatic Excited-State Molecular Dynamics in NWChem: Supporting Information

HUAJING SONG<sup>1,\*</sup>, VICTOR M. FREIXAS<sup>2</sup>, SEBASTIAN FERNANDEZ-ALBERTI<sup>2</sup>,  
ALEXANDER J. WHITE<sup>1</sup>, YU ZHANG<sup>1</sup>, SHAUL MUKAMEL<sup>3</sup>, NIRANJAN GOVIND<sup>4,\*</sup>,  
AND SERGEI TRETIAK<sup>1,5,\*</sup>

<sup>1</sup>Physics and Chemistry of Materials, Theoretical Division, Los Alamos National Laboratory, Los Alamos, New Mexico, 87545, USA

<sup>2</sup>Departamento de Ciencia y Tecnología, Universidad Nacional de Quilmes/CONICET, B1876BXD, Bernal, Argentina

<sup>3</sup>Departments of Chemistry, and physics and astronomy, University of California, Irvine, CA 92697, USA

<sup>4</sup>Physical and Computational Sciences Directorate, Pacific Northwest National Laboratory, Richland, WA 99352, USA

<sup>5</sup>Center for Integrated Nanotechnologies, Los Alamos National Laboratory, Los Alamos, New Mexico 87545, USA

\*Corresponding author: songhw@lanl.gov, niri.govind@pnnl.gov, serg@lanl.gov.

## 1. NUMERICAL ERROR RELATED TO TIME SCALE

Numerical errors can arise in the MCE calculations (between cloning configurations) due to the rapidly changing Ehrenfest amplitudes  $a^{(n)}_I$ , especially in the strong non-adiabatic coupling regions. These errors can be reduced by narrowing the nuclear time steps ( $\Delta t$ ), electronic time steps ( $\delta t$ ), or restricting the number of cloning configurations. Fig.S1 plot the sum of the state population in multi-configuration, which is the norm of the MCE wavefunction for a Formaldimine ( $\text{CH}_2\text{NH}_2^+$ ) system. The testing  $\text{CH}_2\text{NH}_2^+$  MCE-AIMC runs in TDDFT level with B3LYP exchange-correlation functional and STO-3G basis sets. A 1% deviation limit is imposed for the norm (i.e.,  $0.99 \sim 1.01$ ) to ensure conservation in the MCE calculation. As shown in Fig.S1a and b, the numerical errors are reflected by a irregular vibrating of the norm around 1 after the first cloning event (around 6 fs in Fig.S1 a, and 7 fs in Fig.S1b). Narrowing the nuclear time step from 100 a.u. to 1 a.u. can significantly reduced the norm errors by 10 times (see Fig.S1b). However, narrowing the electronic time step in the same factor from  $\Delta t = 1\delta t$  to  $\Delta t = 100\delta t$  at  $\Delta t = 10$  a.u. can only reduced the norm errors by a factor of 2, and decreasing the electronic time step below  $\Delta t = 100\delta t$  will not provide further improvement (see Fig.S1a). Moreover, Fig.S1a also shows that the velocity rescaling thermostat will introduce numerical errors between cloned trajectories.

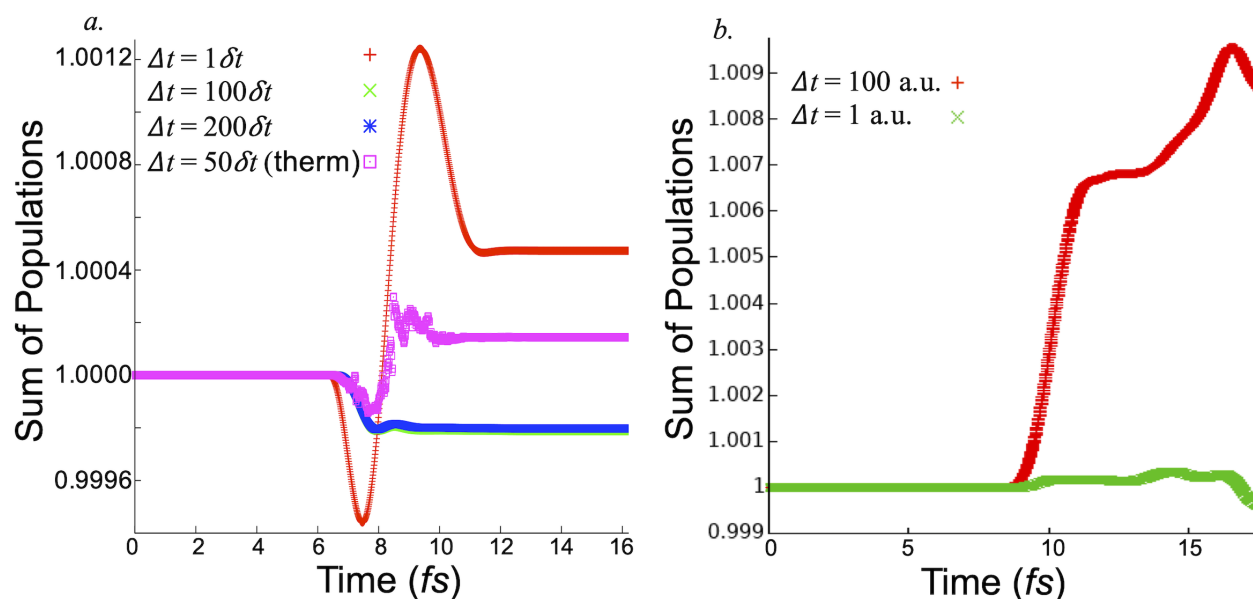


**Fig. S1.** Plot the sum of the state population (norm) in MCE-AIMC run for Formaldimine ( $\text{CH}_2\text{NH}_2^+$ ) molecular system. The deviation of the norm from 1 indicated the numerical errors arise in the MCE calculations. *a.* compare the errors with different electronic time steps setting, and the effect of velocity rescaling thermostat with nuclear time steps set to  $\Delta t = 10$  a.u. *b.* shows the errors in different nuclear time steps setting with electronic time steps set to  $\Delta t = 10\delta t$ .

## 2. COMPARISON WITH STO-3G BASIS SET RESULTS

Figure S2 shows further analysis of criterion 3 (Eq.(28)) with  $\delta = 0.005$  in all four methods used. During the initial 100 fs of MCE-AIMC NAMD simulations, about 70% of the initial trajectories are cloned more than twice, and a significant peak can be observed for 3 - 5 cloning events in all methods. The results for B3LYP functional and both basis sets show a broad distribution of the clonings up to the limit. In contrast, the PBE0 results are centralized around 3 to 4 cloning times with no initial trajectories cloned by more than 8 times. These trends can be tentatively linked to effective gaps between excited states: larger gaps generally indicate smaller interactions between states. Overall, the minimal STO-3G basis sets provides a sufficient testing ground for the cloning criteria that can be further used for higher-level basis sets simulations.

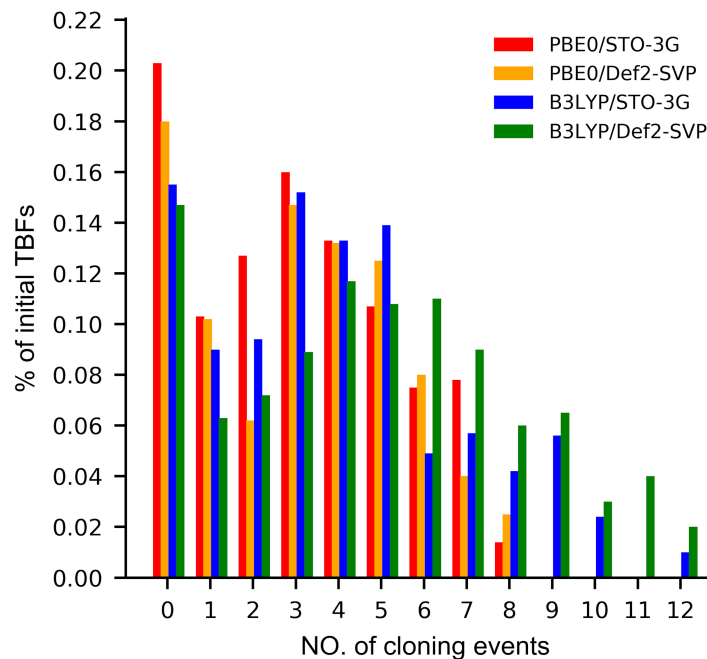
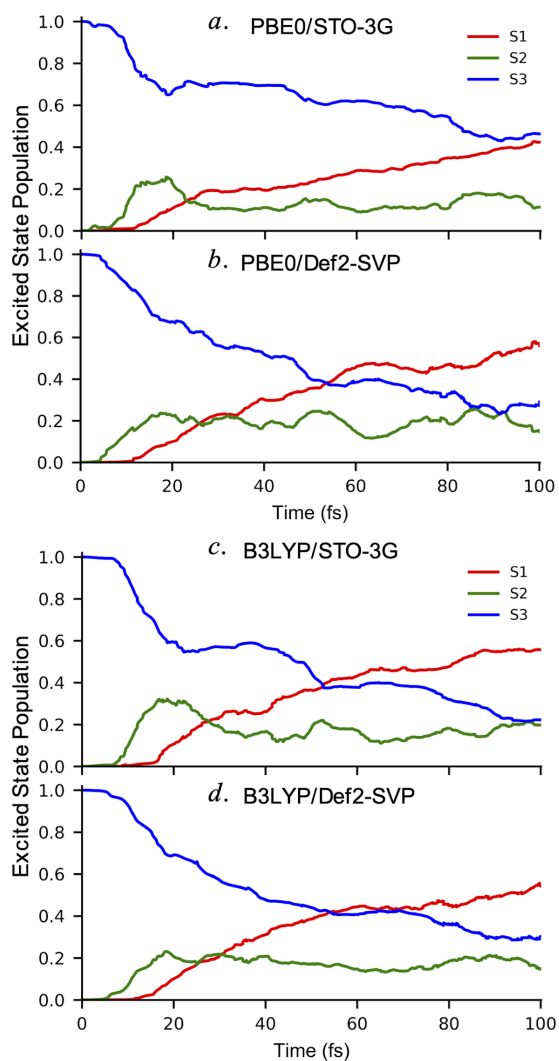


Fig. S2. Distribution of cloning events per original TBFs for different exchange-correlation functionals and basis sets.

Figure S3 compares the time evolution of the average populations for the lowest three electronic excited states evaluated by MCE. Initially, oscillatory population exchange is observed between  $S_3$  and  $S_2$  states up to 80 fs of excitation dynamics, particularly in B3LYP simulations. Such oscillations typically signify the presence of coherent electron-vibrational dynamics. For the STO-3G basis sets, the PBE0 results display faster damping of  $S_3$  to  $S_2$  oscillations, but all results show similar  $S_3$  to  $S_1$  relaxation rates.



**Fig. S3.** Time evolution of the excited state populations calculated using *a.* PBE0/STO-3G, *b.* PBE0/Def2-SVP, *c.* B3LYP/STO-3G, and *d.* B3LYP/Def2-SVP methods.

### 3. EXAMPLE NWChem INPUT

#### 3.1 Example main NWChem input file for AIMC calculation:

```
start nwchem
echo

geometry nocenter noautosym noautoz
C      1.32585502    0.03531395    0.02690052
C      0.68498397   -1.15933347   -0.05185560
C     -0.69477701   -1.18246710   -0.00862880
C     -1.35159135   -0.00892812   -0.04502134
C     -0.61982274    1.21601272    0.04322478
N      0.71513790    1.20982134    0.03307881
H      2.45660877    0.11693516    0.05233766
H      1.29724121   -2.05060387   -0.06469408
H     -1.23238790   -2.12319160    0.03078739
H     -2.44150543   -0.02652987   -0.04755736
H     -1.13852024    2.24939990   -0.00921318
end

basis
  * library Def2-SVP
end

dft
  xc pbe0
  maxiter 200
end

tddft
  nroots 10
  notriplet
  cis
  maxiter 200
  civecs
  grad
  root 1
end

qmd
  nstep_nucl 50
  dt_nucl 0.5
  targ_temp 300.0
  thermostat none
  print_xyz 10
  com_step 100
  rand_seed 425216
  namd aimc
  nstates 5
  init_state 3
  dt_elec 0.01
  decoherence off
  clone_max 12
end

task tddft qmd
```

The initial DFT, TDDFT, and Gaussian Basis adiabatic *ab-initio* molecular dynamics (qmd) setting are identical with the original formats; one can refer to the NWChem User Documentation [1]. We have implemented the new EHR and MCE-AIMC non-adiabatic molecular dynamics (NAMD) as an extension to the quantum molecular dynamics (qmd) module in NWChem. In the namd sub-block within the qmd block, a specific NAMD method (SH, EHR, or AIMC) must be specialized. The keyword nstates sets the number of electronic states to include in the NAMD calculation, i.e., the number of states for use with Eq.6. The number of roots requested in

the tddft block must be at least  $nstates-1$ . The keyword `init_state` sets the initial electronic state to be occupied; the numbering for this keyword and the output that reports the currently occupied state runs from 0 (ground state) to  $nstates-1$ . So if you want to start a calculation in the first excited state, you would set `init_state` to 1. The keyword `dt_elec` sets the electronic time step for Eq.7 (in atomic units). The nuclear time step (`dt_nucl`) must be an integer multiple of the electronic time step ( $\text{mod}(\text{dt\_nucl}, \text{dt\_elec})=0$ ). The decoherence will be automatically set to "none" in the EHR and AIMC calculation. The default maximum number of cloning is 4 for AIMC and 0 for EHR.

## 1.2 Example MCE Observable calculation input file for transition density segments and atomic distances:

To calculate the expected values for specific atomic distance and transition density segments. An extra MCE input file is required.

For interatomic distance:

The number of atom pairs of indexes (`nIndexR`) must be identified then followed by the pairs of atom ID.

For transition density segments:

The number of sections to calculate the transition density must be defined, followed by the number of atomic orbitals (AO) in each section, and finally, the ID of AO.

An example is shown below:

```
!Number of indexes
&Nind
  nIndexR=4 !Pairs of indexes for calculating interatomic distances
  nSectTd=2 !Number of sections to calculate TD
&endNind

!Pairs to calculate distances between atoms
&Pairs
  6 5
  6 1
  3 2
  2 1
&endPairs

!Number of orbitals of each section for calculating TD
&TDNindexes
  42
  42
&endTDNindexes

!Indexes for orbitals of each section for calculating TD
&TDorbitals
  1 2 3 4 5 6 7 8 9 10 11 12 13 14 57 58 59 60 61 62 63 64 65 66 67 68 69 70 71 72 73 74
  75 76 77 78 79 80 81 82 83 84

  15 16 17 18 19 20 21 22 23 24 25 26 27 28 29 30 31 32 33 34 35 36 37 38 39 40 41 42 43
  44 45 46 47 48 49 50 51 52 53 54 55 56
&endTDorbitals
```

#### 4. GROUND STATE OPTIMIZED STRUCTURE OF PYRIDINE

C	1.34875458	0.06611918	-0.00000041
C	0.70880300	-1.17458090	0.00000025
C	-0.68436380	-1.20060034	-0.00000012
C	-1.37184696	0.01127717	0.00000024
C	-0.63046217	1.19421208	-0.00000054
N	0.70026694	1.22874226	0.00000075
H	2.44458330	0.11909444	-0.00000008
H	1.29399541	-2.09765210	-0.00000004
H	-1.22606202	-2.15076176	-0.00000001
H	-2.46425262	0.04395628	0.00000004
H	-1.14316160	2.16416607	-0.00000009

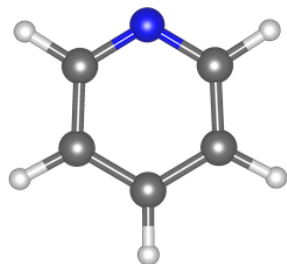


**Fig. S4.** Pyridine (C<sub>5</sub>H<sub>5</sub>N) molecule.

**REFERENCES**

1. E. Apra, E. J. Bylaska, W. A. De Jong, N. Govind, K. Kowalski, T. P. Straatsma, M. Valiev, H. van Dam, Y. Alexeev, J. Anchell *et al.*, “Nwchem: Past, present, and future,” *The J. chemical physics* **152**, 184102 (2020).